

RESEARCH ARTICLE

AP180 promotes release site clearance and clathrin-dependent vesicle reformation in mouse cochlear inner hair cells

Jana Kroll^{1,2,3,4,*}, Özge Demet Özçete^{3,4,5,6,†}, Sangyong Jung^{5,7}, Tanja Maritzen⁸, Ira Milosevic^{1,3}, Carolin Wichmann^{2,3,5,§} and Tobias Moser^{3,5,6,9,§}

ABSTRACT

High-throughput neurotransmission at ribbon synapses of cochlear inner hair cells (IHCs) requires tight coupling of neurotransmitter release and balanced recycling of synaptic vesicles (SVs) as well as rapid restoration of release sites. Here, we examined the role of the adaptor protein AP180 (also known as SNAP91) for IHC synaptic transmission by comparing AP180-knockout (KO) and wild-type mice using high-pressure freezing and electron tomography, confocal microscopy, patch-clamp membrane capacitance measurements and systems physiology. AP180 was found predominantly at the synaptic pole of IHCs. AP180-deficient IHCs had severely reduced SV numbers, slowed endocytic membrane retrieval and accumulated endocytic intermediates near ribbon synapses, indicating that AP180 is required for clathrin-dependent endocytosis and SV reformation in IHCs. Moreover, AP180 deletion led to a high prevalence of SVs in a multi-tethered or docked state after stimulation, a reduced rate of SV replenishment and a hearing impairment. We conclude that, in addition to its role in clathrin recruitment, AP180 contributes to release site clearance in IHCs.

This article has an associated First Person interview with the first author of the paper.

KEY WORDS: AP180, SNAP91, Ribbon synapse, Exocytosis, Endocytosis, Hearing, Electron tomography, Membrane capacitance

INTRODUCTION

Ribbon synapses of inner hair cells (IHCs) of the cochlea with spiral ganglion neurons feature one of the highest rates of continuous

neurotransmitter release in the mammalian body in order to indefatigably encode sound (Pangršič et al., 2012). Hence, hearing requires, on the one hand, the very fast exocytosis of neurotransmitter-containing SVs and, on the other hand, a highly efficient endocytosis and reformation of fusion-competent synaptic vesicles (SVs) to balance the massive SV exocytosis. The specialized structure of the IHC active zone (AZ) – notably the electron-dense ribbon that is made of RIBEYE (an isoform of CtBP2, herein denoted RIBEYE/CtBP2) and tethers a halo of SVs (Jean et al., 2018; Becker et al., 2018; Khimich et al., 2005; Schmitz et al., 2000) – and a unique protein composition of release machinery and AZ cytomatrix are thought to accomplish these tasks (reviewed in Moser et al., 2019; Rutherford and Moser, 2016; Safieddine et al., 2012; Wichmann and Moser, 2015). Interestingly, IHC exocytosis seems to operate without the neuronal soluble *N*-ethylmaleimide-sensitive-factor attachment receptor (SNARE) proteins SNAP25, syntaxin-1 and VAMP2 (Nouvian et al., 2011). Instead, the multi-C₂ domain protein otoferlin, loss or dysfunction of which causes human genetic deafness (Yasunaga et al., 1999), serves as a key molecule in IHC exocytosis. After the onset of hearing in mice, otoferlin is thought to be the Ca²⁺-sensor of exocytosis in IHCs, and also to mediate efficient SV replenishment, possibly by advancing SV tethering and release site clearance (Chakrabarti et al., 2018; Duncker et al., 2013; Johnson and Chapman, 2010; Jung et al., 2015a; Kroll et al., 2019; Michalski et al., 2017; Pangršič et al., 2010; Roux et al., 2006; Strenzke et al., 2016; Vogl et al., 2015, 2016). Clearance of previously exocytosed proteins and lipids from the release sites is considered a critical step in preparing the next round of SV exocytosis (Haucke et al., 2011; Neher and Sakaba, 2008). The action of otoferlin in release site clearance is likely achieved through binding to the adaptor protein 2 (AP-2) (Duncker et al., 2013; Jung et al., 2015a) and/or endophilin A1 (Kroll et al., 2019). Like in neurons (Kononenko et al., 2014), absence of AP-2 from IHCs compromises the clathrin-dependent reformation of SVs from endosome-like vacuoles (ELVs), but, surprisingly, does not significantly impair endocytic membrane retrieval (Jung et al., 2015a).

Endocytic membrane retrieval in IHCs comprises a slow, linear component that likely reflects clathrin-mediated endocytosis (CME), and a fast, exponential component thought to represent bulk retrieval (Moser and Beutner, 2000; Neef et al., 2014). Morphological evidence for CME and bulk retrieval in hair cells has been reported previously (e.g. Jung et al., 2015a; Lenzi et al., 2002; Neef et al., 2014; Siegel and Brownell, 1986). Molecular entities identified to mediate SV recycling in hair cells include dynamins, endophilin-As, clathrin and synaptojanin-1 (Boumil et al., 2010; Jung et al., 2015a; Kroll et al., 2019; Neef et al., 2014; Trapani et al., 2009). Their disruption primarily affects the slow component of IHC membrane retrieval, that is, CME. So far, little is known about whether the molecular regulation of bulk retrieval at hair cell synapses is similar to that described for other synapses and neuroendocrine cells (for reviews, see Cousin, 2017; Wu et al., 2014).

¹Synaptic Vesicle Dynamics Group, European Neuroscience Institute Göttingen – A Joint Initiative of the University Medical Center Göttingen and the Max-Planck-Society, 37077 Göttingen, Germany. ²Molecular Architecture of Synapses Group, Institute for Auditory Neuroscience, InnerEarLab and Center for Biostructural Imaging of Neurodegeneration, University Medical Center Göttingen, 37075 Göttingen, Germany. ³Collaborative Research Center 889, University of Göttingen, 37075 Göttingen, Germany. ⁴Göttingen Graduate School for Neuroscience and Molecular Biosciences, University of Göttingen, 37075 Göttingen, Germany. ⁵Institute for Auditory Neuroscience and InnerEarLab, University Medical Center Göttingen, 37075 Göttingen, Germany. ⁶Auditory Neuroscience Group, Max Planck Institute of Experimental Medicine, 37075 Göttingen, Germany. ⁷Neuro Modulation and Neuro Circuitry Group, Singapore Bioimaging Consortium (SBIC), Biomedical Sciences Institutes, 138667 Singapore. ⁸Leibniz-Forschungsinstitut für Molekulare Pharmakologie (FMP), 13125 Berlin, Germany. ⁹Synaptic Nanophysiology Group, Max Planck Institute for Biophysical Chemistry, 37077 Göttingen, Germany. *Present address: Institute of Neurophysiology, Charité-Universitätsmedizin, 10117 Berlin, Germany. †These authors contributed equally to this work

§Authors for correspondence (carolin.wichmann@med.uni-goettingen.de; tmoser@gwdg.de)

© J.K., 0000-0003-4243-4088; T.M., 0000-0003-4993-0340; I.M., 0000-0001-6440-3763; C.W., 0000-0001-8868-8716; T.M., 0000-0001-7145-0533

A further dissection of the molecular physiology of IHC SV recycling is key to comprehending indefatigable sound encoding. In this context, the neuronal endocytic adaptor protein AP180 is an interesting candidate protein. Through binding of clathrin, AP-2 and the phospholipid phosphatidylinositol 4,5-bisphosphate [PI(4,5)P₂], AP180 was shown to be involved in the early steps of clathrin-coated pit (CCP) formation in neurons (Ford et al., 2001; Hao et al., 1999; Lindner and Ungewickell, 1992; Morris et al., 1993; Moshkanbaryans et al., 2016). In AP180-knockout (AP180-KO) mice, accumulations of ELVs and lower numbers of clathrin-coated structures have been observed, underlining the importance of AP180 for CME as well as for clathrin-dependent SV reformation from ELVs (Koo et al., 2015). Through its AP180 N-terminal homology (ANTH) domain, AP180 binds to the SNARE domain of VAMP2 and other members of the VAMP family (Koo et al., 2011; Maritzen et al., 2012). This way, AP180, as well as its ubiquitously expressed homolog CALM, organize the recycling of VAMP2 from the plasma membrane after SNARE complex disassembly following SV fusion and, thereby, contribute to the clearance of release sites in neurons (Koo et al., 2011; 2015; Maritzen et al., 2012; Miller et al., 2011). AP180-dependent clearance of release sites seems to be of greater importance in inhibitory neurons that show higher rates of transmitter release than excitatory neurons (Koo et al., 2015). However, the relevance of AP180 for high-throughput synaptic transmission of sensory ribbon synapses is unclear, especially at IHCs, which seem to operate without the AP180 cargo protein VAMP2 (Nouvian et al., 2011).

Here, we studied the role of AP180 at murine IHC ribbon synapses from the molecular to the systems level. By combining confocal microscopy, chemical depolarization of IHCs, high-pressure freezing and electron tomography, perforated patch-clamp, and recordings of otoacoustic emissions and auditory brainstem responses, we discovered that AP180 has a role in release site clearance and clathrin assembly for CME, as well as in SV reformation following bulk retrieval in IHCs, and thereby is important for hearing.

RESULTS

AP180 is present at IHC synapses of the murine cochlea and redistributes upon stimulation

First, we aimed to identify whether the adaptor protein AP180 is present in the murine organ of Corti, and, more specifically, in IHCs. Therefore, we performed immunohistochemistry in apical cochlear turns (~2–12 kHz) of wild-type (Wt) mice acutely explanted after the onset of hearing, as well as of age-matched AP180-KO mice (used as a control for antibody specificity). We immunostained for AP180 in combination with markers for efferent synapses [synapsin 1 and 2 (synapsin 1/2); note that IHCs do not contain synapsin 1/2], the synaptic ribbon (RIBEYE/CtBP2), and hair cells (otoferlin). Immunofluorescence (Fig. 1A, left panel) revealed the presence of AP180 in IHCs and outer hair cells (OHCs), as well as in efferent synapses underneath the hair cells and possibly in spiral ganglion neurons (see their somata in the inset to Fig. 1A). A lack of AP180 staining in organs of Corti from AP180-KO mice confirmed the high specificity of the AP180 antibody (Fig. S1A). Higher magnifications of maximum intensity *z*-projections (Fig. 1A, right panel) revealed that AP180 is most prevalent in the basal half of IHCs where the ribbon synapses are located ('synaptic pole'). Single *xy*-sections through the synaptic pole of immunolabeled IHCs show an intracellular as well as plasma membrane distribution of AP180. Line profiles through the longitudinal axis of IHCs (Fig. 1B_{ii}) revealed that the highest fluorescence intensity levels were at the IHC plasma membrane, followed by the IHC lumen and efferent presynaptic terminals.

The distribution of AP180 immunofluorescence was altered upon high-K⁺ depolarization (65 mM for 1 min, Fig. S1B). Compared to in the resting condition, the average intensity of AP180 fluorescence was significantly reduced in a distance of 2 μm from the plasma membrane (Fig. S1C_{ii}; *P*=0.0003, unpaired Student's *t*-test) after high-K⁺ stimulation, whereas the staining near the membrane was preserved (Fig. S1C_i; *P*=0.5468, unpaired Student's *t*-test). We further observed that high-intensity AP180 immunofluorescence clusters were already present in the proximity of the plasma membrane at the synaptic pole in the resting condition, but appeared even more intense after stimulation (Fig. S1B_i). While the size of the clusters did not differ after 1 min of high-K⁺ stimulation compared to in the resting condition (Fig. S1D; *P*=0.105, Mann–Whitney *U*-test), we found a higher mean intensity of AP180 immunofluorescence clusters after stimulation (Fig. S1D_i; *P*<0.0001, Mann–Whitney *U*-test). These data indicate a stimulation-induced recruitment of AP180 to the plasma membrane, pointing towards a relevance of AP180 for IHC synaptic transmission.

AP180 is required for normal hearing

In order to probe for a function of AP180 in IHC synaptic transmission at the systems level, we recorded auditory brainstem responses (ABRs) and distortion product otoacoustic emissions (DPOAEs). Wt and AP180-KO mice showed comparable ABR wave amplitudes (Fig. 2A,D) and ABR latencies (Fig. 2E), while the ABR thresholds were modestly but significantly increased in the AP180-KO mice (Fig. 2B; *P*<0.01, two-way ANOVA followed by post-hoc Tukey's test). DPOAEs, reflecting cochlear amplification, were intact in AP180-KO mice, which reveals normal mechano-electrical transduction and electromotility of OHCs (Fig. 2C). Therefore, we conclude that the elevation of ABR thresholds arises from a dysfunction downstream of mechano-electrical transduction and cochlear amplification, that is, in IHCs, their synapses or the auditory pathway.

AP180 absence alters the levels of Vglut3, but not of otoferlin

In IHCs of mice with a knockout of the AP-2 subunit AP-2μ (also known as AP2M1), otoferlin levels are known to be strongly reduced, with the reduction being less pronounced at the plasma membrane, suggesting impaired sorting of otoferlin (Jung et al., 2015a). Therefore, we tested by semi-quantitative analysis of otoferlin immunofluorescence if deletion of AP180 likewise changes otoferlin levels and/or distribution (Fig. 3A,A_i). Yet, neither otoferlin distribution, nor total fluorescence intensity, were altered in IHCs of AP180-KO mice compared to Wt (*P*=0.17, unpaired Student's *t*-test). However, we noted that the immunofluorescence intensity of the vesicular glutamate transporter of IHCs, Vglut3 (also known as SLC17A8), was reduced by 17.1±3.2% (mean±s.e.m.) throughout the IHC in AP180-KO mice compared to Wt (Fig. 3B,B_i; *P*<0.0001, unpaired Student's *t*-test). However, quantitative PCRs of AP180-KO and control (Wt and heterozygote) mice [postnatal day (P)12–P14] revealed that mRNA levels of otoferlin and Vglut3 remained unchanged (Fig. S2). Notably, co-staining for RIBEYE/CtBP2 and Homer1 (a marker for the postsynaptic density; Fig. 3C) indicated an unaltered ribbon anchorage to the AZ as well as a normal number of ribbon synapses (Fig. 3C_i; ribbon synapses per IHC for Wt: 14.5±0.4, for AP180-KO: 14.5±0.5 synapses per IHC; *P*=0.96, unpaired Student's *t*-test; mean±s.e.m.) in AP180-KO mice. In summary, deletion of AP-180 did not alter otoferlin levels, synapse number or ribbon anchorage, but it reduced Vglut3 protein levels, potentially via diminishing SV numbers.

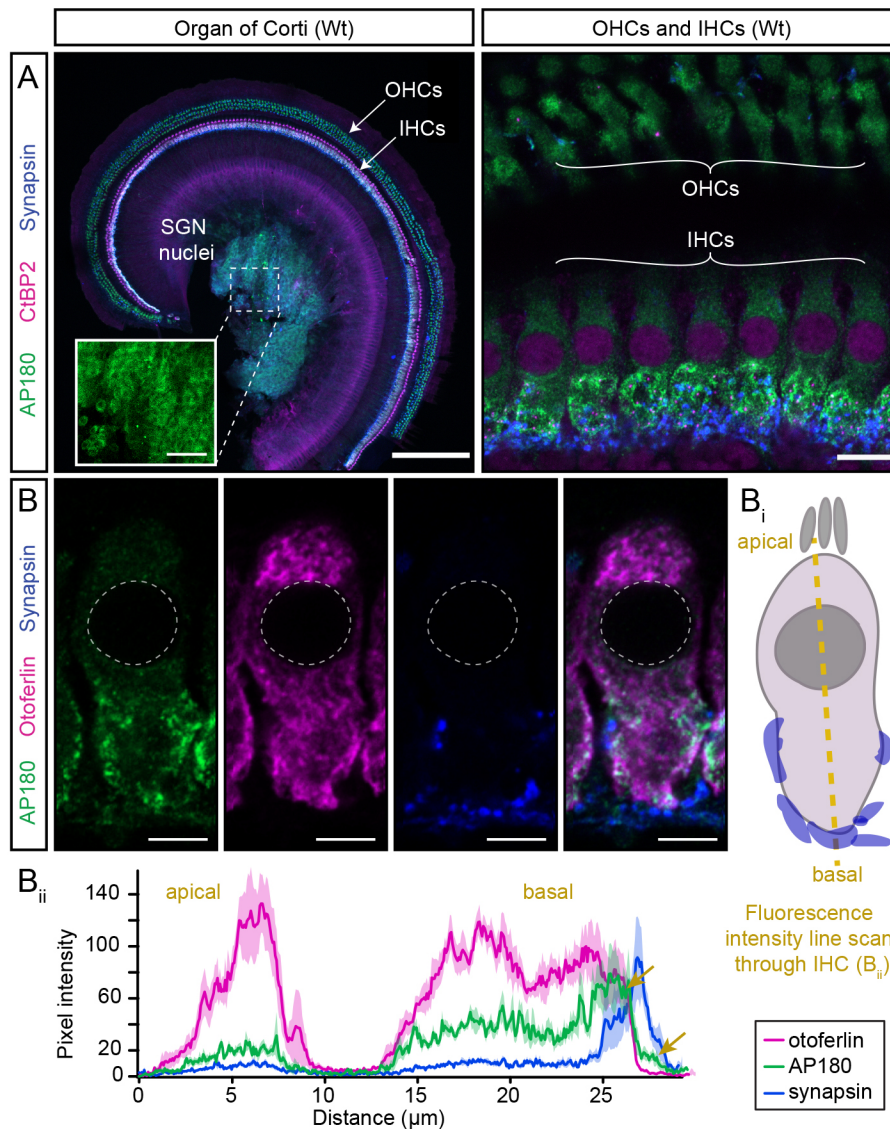


Fig. 1. AP180 is present in the murine organ of Corti. (A) Maximum intensity z-projection of confocal sections of an apical cochlear turn (left) and higher magnification of IHCs and OHCs (right) from a P15 Wt animal immunolabeled for AP180, RIBEYE/CtBP2 (staining ribbons and nuclei) and synapsin1/2 (found in the nerve terminals of lateral olivocochlear efferents, but not in IHCs). Scale bars: 200 μm (left); 50 μm (inset left); 10 μm (right). The inset in A represents a magnification into the spiral ganglion area and shows AP180 immunofluorescence in the somata of spiral ganglion neurons. (B) Single confocal sections from a synaptic pole of an IHC (Wt, P15) using markers for AP180, otoferlin and synapsin1/2. Scale bars: 5 μm. (B_i,B_{ii}) Average fluorescence intensity line profiles through the longitudinal axis of seven IHCs from apical to basal. AP180 fluorescence is strongest in proximity to the IHC basal membrane, as indicated by yellow arrows (thereby overlapping with the otoferlin signal), but can also be detected in efferent nerve terminals (overlapping with the synapsin1/2 signal) and potentially in the postsynaptic boutons of spiral ganglion neurons.

The numbers of SVs and clathrin-coated structures are reduced in IHCs of AP180-KO mice

Next, we performed high-pressure freezing followed by freeze substitution and electron tomography of ribbon synapses from P15–P16 mice (shortly after the onset of hearing) to assess the synaptic ultrastructure. Exemplary virtual sections (Fig. 4A), obtained from semi-thin sections via tomogram generation, as well as 3D models of reconstructed ribbon synapses from Wt and AP180-KO IHCs (Fig. 4B) revealed reduced numbers of SVs not only in direct vicinity to the ribbon, but also in the cytoplasm. We investigated the following three morphological pools of SVs, as defined previously (Kroll et al., 2019) and as indicated in the schematic drawing (Fig. 4D): (1) ribbon-associated SVs (RA-SVs) in a maximum distance of 80 nm to the ribbon, (2) membrane-proximal SVs (MP-SVs) that are within a 50 nm distance from the plasma membrane and 100 nm laterally from the presynaptic density, and (3) cytosolic SVs (operationally defined as all uncoated vesicles with a maximum outer diameter of 70 nm and a maximum distance of 500 nm from the ribbon, excluding the aforementioned SV pools). In all three pools, numbers of SVs were reduced in IHCs of AP180-KO mice compared to Wt. The strongest reduction, of ~60%, was observed for the pool of cytosolic SVs (Fig. 4I; $P < 0.0001$, unpaired Student's

t-test). Numbers of RA-SVs (Fig. 4E; $P = 0.0062$, unpaired Student's *t*-test) and of MP-SVs (Fig. 4F; $P = 0.0328$, unpaired Student's *t*-test) were reduced by ~24% and 22%, respectively. The reduction of SVs, found in electron tomography, exceeded the expectation based on Vglut3 immunofluorescence (reduction by ~17%). The outer diameter of the cytosolic SVs, on the other hand, was increased on average (Fig. 4J; $P < 0.0001$, unpaired Student's *t*-test) and more variable in IHCs of AP180-KO mice compared to Wt ($P < 0.0001$, Kolmogorov–Smirnov test), which may account for the modest reduction of Vglut3 fluorescence intensity. The observed increase of the SV diameter is consistent with results of previous studies on mice and invertebrates missing AP180 or its homolog UNC-11 (Koo et al., 2015; Nonet et al., 1999; Vanlandingham et al., 2014; Zhang et al., 1998). Interestingly, the average distance of MP-SVs to the AZ plasma membrane was slightly increased in IHCs from AP180-KO mice compared to Wt (Fig. 4G; $P = 0.0288$, Mann–Whitney *U*-test).

We further quantified the numbers of clathrin-coated structures in proximity to the ribbon, including coated vesicles and coated pits budding from the plasma membrane or from ELVs, examples of which can be seen in Fig. 4C. The numbers of coated structures in total (Fig. 4H; $P = 0.0002$, unpaired Student's

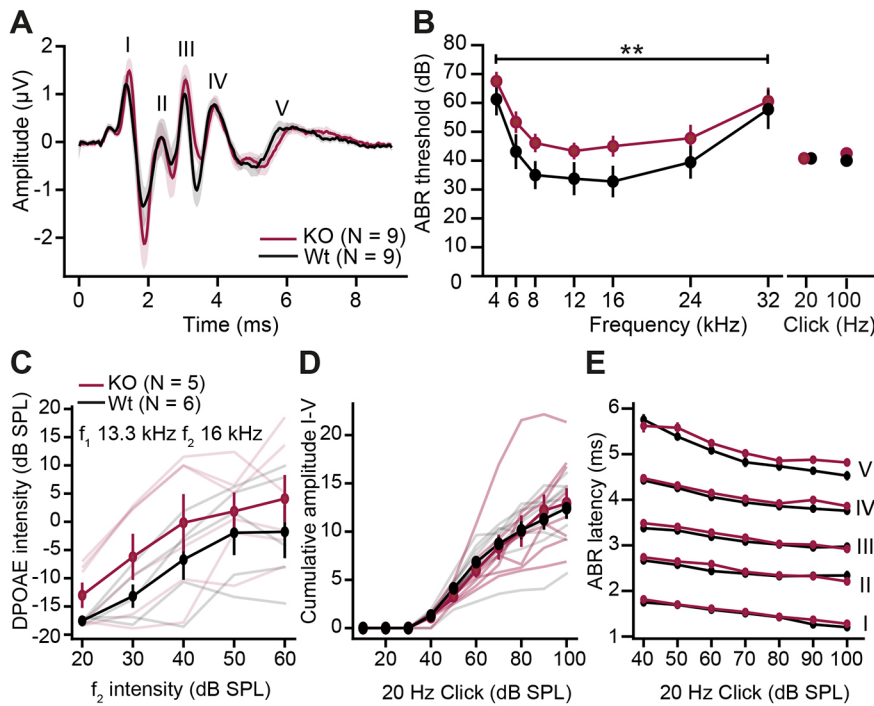


Fig. 2. Auditory brainstem responses show elevated thresholds in AP180-KO mice. (A) ABR waveforms were recorded in response to 80 dB clicks [mean±s.e.m., AP180-KO N (number of mice)=9, Wt N=9]. Roman numerals (I–V) indicate the ABR waves. (B) ABR thresholds were significantly elevated for AP180-KO mice compared to Wt mice (mean±s.e.m., AP180-KO N=9, Wt N=9). ***P*<0.01 (two-way ANOVA followed by post-hoc Tukey’s test). Click thresholds (for 20 and 100 Hz) remained unchanged. (C) DPOAE amplitudes (mean±s.e.m.) recorded in response to the pair of simultaneous sine waves (f₁=13.3 kHz and f₂=16 kHz) at increasing intensity (f₂ intensity was 10 dB bigger than f₁ intensity) were unaltered. (D) The cumulative amplitude from wave 1 to 5 was comparable in AP180-KO and Wt mice. (E) Latencies of ABR waves I–V did not show any difference in AP180-KO mice compared to Wt mice. Results from individual mice are shown as fainter lines in C and D.

t-test), and of coated vesicles in particular (*P*<0.0001, Mann–Whitney *U*-test, please also see Table S1 for further information on statistical analyses), were strongly reduced in AP180-KO mice

compared to Wt. This suggests an involvement of AP180 in the early steps of clathrin-mediated membrane retrieval. While numbers of ELVs were not significantly increased in tomograms

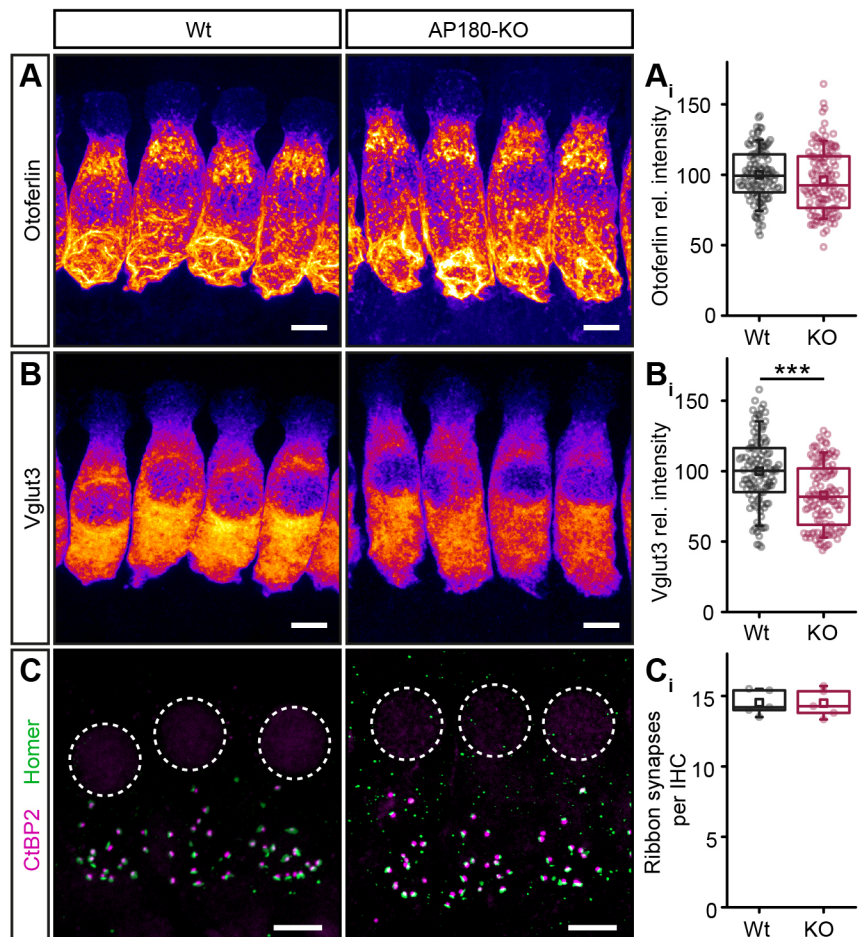


Fig. 3. Reduced Vglut3 levels, but unaltered otoferlin levels in AP180-deficient IHCs. (A) Maximum intensity z-projections of otoferlin-stained apical cochlear turns from AP180-KO and Wt littermate controls. (A_i) Unaltered otoferlin levels in AP180-KO (*n*=114 IHCs from *N*=4 mice) compared to Wt (*n*=107 IHCs from *N*=4 mice). (B) Maximum intensity z-projections of confocal sections of Wt and AP180-KO IHCs stained for Vglut3. (B_i) Intracellular Vglut3 levels were reduced by ~17% in AP180-KO IHCs (*n*=114 IHCs from *N*=4 mice) compared to Wt (*n*=107 IHCs from *N*=4 mice). (C) Exemplary confocal sections of RIBEYE/CtBP2 (magenta) labeling the synaptic ribbon and Homer1 (green) staining labeling the postsynaptic density. Dashed circles highlight the nuclei. (C_i) Equal numbers of ribbon synapses in Wt (six images from three animals, with ~10 cells per image) and in AP180-KO (six images from three animals, with ~10 cells per image). ****P*<0.001. Scale bars: 5 µm.

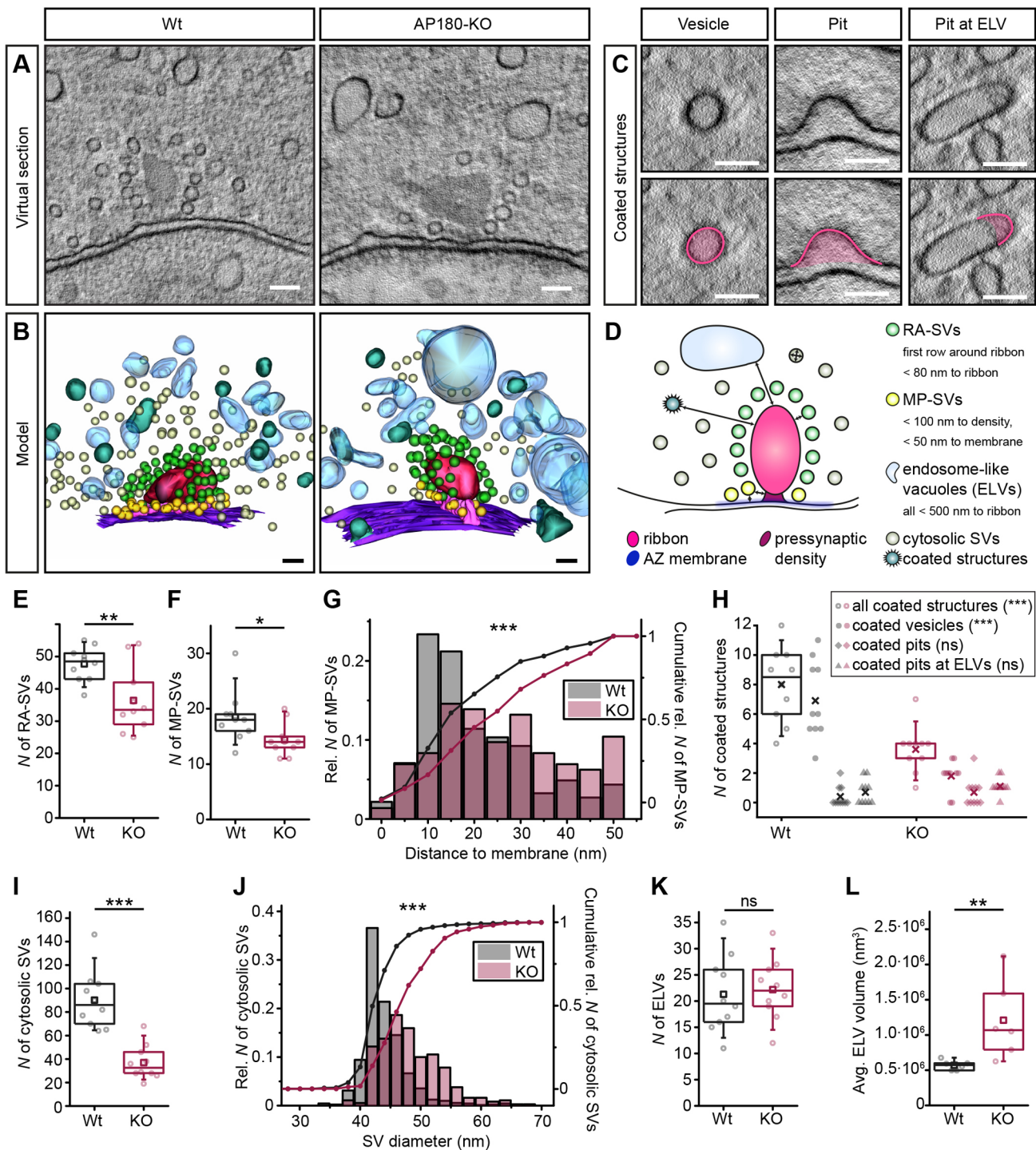


Fig. 4. Ultrastructural changes of IHC ribbon synapses in AP180-KO mice. (A) Representative virtual sections of tomograms from P15 Wt and AP180-KO ribbon synapses. Scale bars: 100 nm. (B) Reconstructed models of the area around the ribbon from P15 Wt and AP180-KO IHCs. Scale bars: 200 nm. (C) Exemplary coated structures observed at the IHC base. Scale bars: 100 nm. (D) Schematic drawing illustrating parameters for the quantifications shown in E–L; $n=10$ tomograms for all quantifications from two different animals in each group. (E) Numbers (N) of RA-SVs were reduced by $\sim 24\%$ in AP180-KO mice. (F) The number of MP-SVs was likewise reduced, and (G) the distance of MP-SVs to the AZ plasma membrane was increased. (H) Numbers of coated structures were decreased with the number of coated vesicles being most strongly affected. (I) In the cytosol, numbers of small uncoated vesicles were drastically ($>60\%$) reduced in the absence of AP180. (J) The average diameter of cytosolic SVs was increased. Generally, SV diameters were more heterogeneous in absence of AP180. (K) Numbers of ELVs were unaltered, (L) while the average volume per ELV was strongly increased in AP180-KO mice. * $P<0.05$; *** $P<0.001$; ns, not significant.

of AP180-KO mice (Fig. 4K; $P=0.7645$, unpaired Student's t -test), we found a strong increase in their average volume (Fig. 4L; $P=0.0043$, Mann–Whitney U -test). Therefore, it is likely that the

reduced numbers and increased size of SVs are a consequence of impaired clathrin- and AP180-dependent SV reformation from ELVs.

IHCs from AP180-KO mice show normal Ca^{2+} influx but impaired SV replenishment

In order to test for the physiological correlates of the morphological changes observed in the AP180-KO IHCs, we performed perforated patch-clamp experiments soon after the onset of hearing (5 mM $[\text{Ca}^{2+}]_e$, P14–P18) in acutely explanted apical cochlear coils (~6–10 kHz). We recorded whole-cell $\text{Ca}_v1.3$ -mediated Ca^{2+} influx in response to step depolarizations of 10 ms from -84 mV to $+63$ mV in 5 mV increments (Fig. 5A, inset). The amplitude of the Ca^{2+} influx of AP180-KO IHCs was statistically indistinguishable from that of Wt IHCs (Fig. 5A). Furthermore, we performed measurements of membrane capacitance increments (ΔC_m), which reports exocytosis evoked by the Ca^{2+} influx. SV pool dynamics were probed by a train of stimuli that consisted of ten step depolarizations to -14 mV of 20 ms duration each, with 150 ms inter-stimuli intervals (Fig. 5B). No significant differences of ΔC_m in response to the first depolarization, which is thought to represent fusion of the readily releasable pool (RRP) of SVs, or in response to the full train of stimuli, were observed (Fig. 5B_i, B_{ii}). We further examined the replenishment rate of the SVs by using the ‘SMN analysis’ (Schneeggenburger et al., 1999). We plotted the cumulative ΔC_m versus the stimulus number and fitted a line for the final five stimuli (Fig. 5C). The obtained apparent replenishment rate (fF/stimulus) was significantly lower in AP180-KO IHCs (Fig. 5C_i, $P=0.037$, unpaired Student’s *t*-test). The increased SV size observed in AP180-KO mice leads to an overestimation of the true rate of SV replenishment. Assuming a spherical SV shape and a specific capacitance of 9.1 fF/ μm^2 (Albillos et al., 1997), we estimated the expected capacitance added by single SV fusion (SV diameter was obtained from the tomograms; Fig. 4J). The mean estimated outer SV diameter values were 44.0 ± 0.1 nm and 48.4 ± 0.3 nm (mean \pm s.e.m.), for Wt and AP180-KO IHCs, respectively. We subtracted the average membrane thickness (6.2 nm, Neef et al., 2007) to obtain the mid-membrane diameter, which is relevant for calculating the capacitance increase upon single SV fusion. The estimated capacitance for Wt SVs (41.3 ± 0.3 aF) was close to the measured value of 40 aF (Grabner and Moser, 2018), while the SV capacitance predicted for AP180-KO IHCs amounted to 51.8 ± 0.7 aF. Based on these estimates, we converted the apparent SV replenishment rate (fF/stimulus, see above) into number of vesicles per stimulus. This revealed a strong impairment in the SV replenishment rate in AP180-KO IHCs (Fig. 5C_{ii}, $P=0.001$, unpaired Student’s *t*-test). Potential reasons for the observed reduction of the replenishment rate in AP180-KO IHCs include (1) deficits in SV docking and/or priming, (2) disturbed release site clearance and (3) impaired SV resupply, including SV reformation and recruitment of SVs to the AZ, which we aimed to decipher in the following experiments.

Deletion of AP180 impairs CME and clathrin-dependent SV reformation in IHCs

Given the role of AP180 in CME and clathrin-dependent SV reformation at conventional synapses (Koo et al., 2015; Zhang et al., 1998), we investigated endocytic membrane retrieval in IHCs of AP180-KO mice. By performing perforated-patch recordings, we determined the endocytic C_m decline following exocytosis in response to step depolarizations to -14 mV for 20 ms and for 200 ms (Neef et al., 2014). As above, both AP180-KO and Wt IHCs showed comparable exocytic ΔC_m upon 20 ms and 200 ms step depolarizations (Fig. 6A,B). The slow and linear component of endocytosis, likely to reflect CME (Neef et al., 2014), dominated the endocytic C_m decline following 20 ms depolarizations in IHCs of

both genotypes (Fig. 6C,E,F). The slope of the linear component was significantly smaller in AP180-KO IHCs compared to Wt IHCs, indicating a deficit in CME (Fig. 6F, $P=0.043$, Mann–Whitney *U*-test). In contrast, the slope of the linear component was comparable between AP180-KO and Wt IHCs upon 200 ms step depolarization (Fig. 6G). Furthermore, AP180 deletion did not impair the fast, exponential component of the endocytosis elicited by exocytosis in response to 200 ms depolarization (Fig. 6D,H,I), which likely reflects bulk endocytosis (Neef et al., 2014).

In a next step, we stimulated freshly dissected P15–P16 organs of Corti for 5 min using high- K^+ followed by high-pressure freezing, freeze substitution and electron tomography (Fig. 7). Similar to what is found in resting conditions, we observed a lower total number of coated structures in IHCs of AP180-KO mice (Fig. 7I, $P=0.002$, Mann–Whitney *U*-test). We detected several ELVs with multiple budding CCPs in proximity to ribbon synapses in Wt, indicative of active SV reformation following bulk endocytosis (examples are shown in the virtual section and in the 3D model in Fig. 7C). However, in AP180-KO mice, we did not observe ELVs with more than one or two budding CCPs. Moreover, the number of ELVs with one or more budding CCPs was reduced in AP180-KO IHCs compared to Wt (Fig. 7I; $P=0.006$, Mann–Whitney *U*-test, also see Table S1). As seen at rest, the total number of ELVs was unaltered in AP180-KO IHCs compared to Wt ($P=0.113$, Student’s *t*-test; Table S1) whereas the average ELV volume was again increased (Fig. 7H; $P=0.0355$, Mann–Whitney *U*-test).

The number of cytosolic SVs was decreased by more than 40% in AP180-KO IHCs (Fig. 7F; $P=0.0026$, Mann–Whitney *U*-test), and, hence, did not go beyond the reduction found at resting conditions. Interestingly, we neither observed a difference in the number of RA-SVs (Fig. 7D; $P=0.445$, Mann–Whitney *U*-test) nor in the number of MP-SVs (Fig. 7E; $P=0.721$, Mann–Whitney *U*-test) between Wt and AP180-KO mice after stimulation. These data indicate that AP180- and clathrin-dependent reformation of SVs is required for maintaining high numbers of cytosolic SVs in the synaptic pole of the IHC. Still, even in absence of AP180, endocytic SV recycling was sufficient to provide enough SVs for refilling the pools of RA-SVs and MP-SVs. Therefore, the role of AP180 in CME and SV reformation seems unlikely to fully account for the observed impairment in SV replenishment.

After stimulation, SVs remain in a multi-tethered state at the AZ of AP180-KO IHCs

In order to investigate potential mechanisms underlying impaired SV replenishment, we further examined the MP-SV pool by electron tomography (Fig. 7A,B). As mentioned above (Fig. 4G), the distance of MP-SVs to the AZ membrane was increased in AP180-KO IHCs under resting conditions. After stimulation, we did not observe significant differences in the average distance to the AZ membrane for MP-SVs between Wt and AP180-KO IHCs (Table S1; $P=0.451$, unpaired Student’s *t*-test). Since SV tethering to the AZ membrane has been suggested to influence the distance between MP-SVs and AZ membrane (e.g. Chakrabarti et al., 2018; Fernández-Busnadiago et al., 2013), we quantified the numbers of tethers to the AZ membrane under resting conditions and after stimulation. For that purpose, we defined the following SV groups: (1) SVs without such tethers, (2) SVs with a single tether, (3) SVs with multiple tethers, and (4) docked SVs, where the distance between SV outer membrane and AZ membrane was 0–2 nm in electron tomography virtual sections, as previously described for IHCs and neurons (Chakrabarti et al., 2018; Imig et al., 2014).

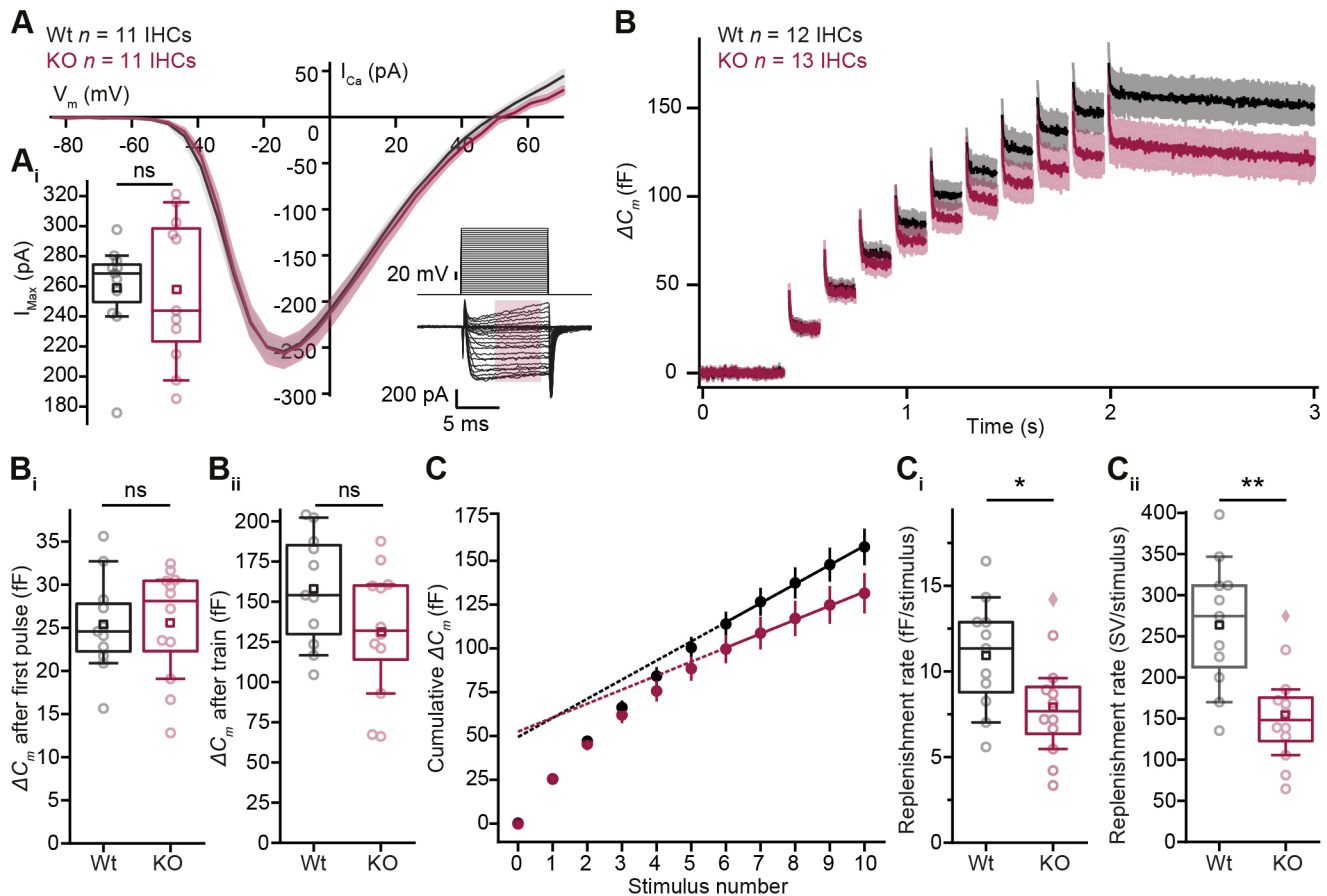


Fig. 5. Impaired SV replenishment, but normal Ca^{2+} influx and SV fusion in AP180-KO IHCs. (A) In order to quantify whole-cell Ca^{2+} current, IHCs were step depolarized for 10 ms from -84 mV to $+63$ mV in 5 mV increments. AP180-KO IHCs showed comparable Ca^{2+} currents to Wt IHCs (AP180-KO $n=11$ IHCs, $N=9$ mice; Wt $n=11$ IHCs, $N=7$ mice) (Ai). The inset shows example Ca^{2+} currents in response to the stimuli paradigm shown above. (B) IHCs were depolarized with a train of stimuli that consists of 10 step depolarizations with durations of 20 ms separated by 150 ms (mean \pm s.e.m., AP180-KO $n=13$ IHCs, $N=9$ mice; Wt $n=12$ IHCs, $N=8$ mice). AP180-KO IHCs had comparable ΔC_m in response to the first stimulus (Bi), and to the train of stimuli (Bii). (C) Cumulative ΔC_m versus stimulus number. A line was fitted to the final five points of the train of stimuli. The replenishment rate estimates (fF/stimulus) were calculated from the slope. (Ci) AP180-KO IHCs showed a significantly slower replenishment rate (fF/stimulus) compared to Wt IHCs (AP180-KO $n=13$ IHCs, $N=9$ mice; Wt $n=12$ IHCs, $N=8$ mice, with the outliers, $P=0.037$, without the outliers, $P=0.01$, Student's t -test). (Cii) Further calculation was performed by taking into consideration the diameter of the SVs obtained from the EM data (Fig. 4J). The replenishment rate of SVs (vesicles/stimulus) was significantly reduced in AP180-KO IHCs compared to Wt IHCs (AP180-KO $n=13$ IHCs, $N=9$ mice; Wt $n=12$ IHCs, $N=8$ mice, with the outliers, $P=0.001$, without the outliers $P=0.0003$, Student's t -test). The outliers were detected via inter-quartile range (IQR) method and are depicted as filled diamonds in box plots. * $P<0.05$; ** $P<0.01$; ns, not significant.

In resting conditions, we did not observe any significant differences in the tethering of MP-SVs in AP180-KO IHCs compared to what was found in the Wt situation (Fig. 7G, one-way ANOVA followed by Tukey's post-hoc test; for individual P -values see Table S1). In line with a previous study of IHCs, high- K^+ stimulation resulted in relatively more tethered SVs (Chakrabarti et al., 2018). This was the case in both Wt and AP180-KO IHCs (Fig. 7G; for the fraction of untethered SVs, resting Wt versus stimulated Wt $P=0.001$, resting Wt versus stimulated AP180-KO $P=0.001$, one-way ANOVA followed by Tukey's post-hoc test). However, we noticed a shift towards an increase in multi-tethered SVs in AP180-KO IHCs after stimulation, whereas most SVs in stimulated Wt IHCs remained connected via a single tether ($P=0.008$ for the fraction of multi-tethered MP-SVs in stimulated Wt versus stimulated AP180-KO IHCs). Furthermore, we observed significantly more docked SVs in stimulated AP180-KO IHCs compared to resting conditions (Wt resting condition versus AP180-KO stimulated condition: $P=0.004$, one-way ANOVA followed by Tukey's post-hoc test; AP180-KO resting versus AP180-KO stimulated: $P=0.002$, one-way ANOVA followed by Tukey's

post-hoc test), as well as compared to stimulated Wt ($P=0.037$, one-way ANOVA followed by Tukey's post-hoc test). Together, these observations indicate that MP-SVs in IHCs of AP180-KO mice remain in the multi-tethered or docked state prior to fusion, which has previously been designated as a morphological correlate of impaired release site clearance in IHCs (Chakrabarti et al., 2018).

DISCUSSION

In the present study, we addressed a role of the endocytic adaptor protein AP180 in synaptic sound encoding in the cochlea. There, IHC ribbon synapses must sustain high rates of SV release for reliable transmission of auditory information. When investigating IHC ribbon synapses of AP180-KO mice by performing a combination of functional patch-clamp recordings, electron tomography and systems physiology, we found evidence for a dual function of AP180. Firstly, AP180 is required for clathrin-dependent SV reformation from ELVs and aids in the early steps of classical CME. Secondly, AP180 plays a role in efficient replenishment of SVs to the release site, likely via promoting the clearance of the release site from proteins and lipids added by preceding SV fusion events.

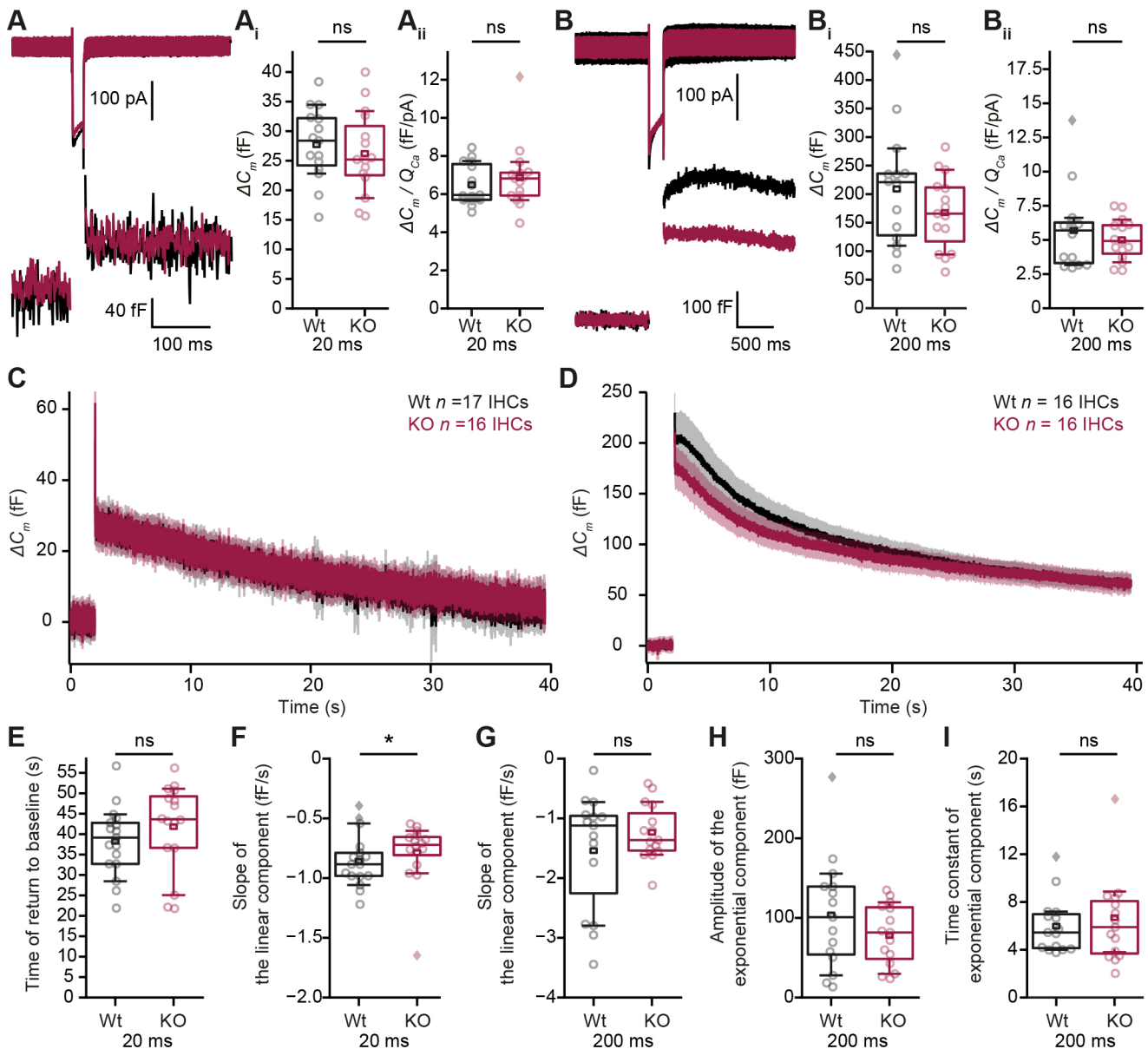


Fig. 6. A reduced rate of the slow component of endocytic membrane retrieval, but intact fast endocytosis in AP180-KO IHCs. (A) Exemplary traces of Ca^{2+} current (top) and capacitance (bottom) upon 20 ms step depolarization to -14 mV from the holding potential of -84 mV. AP180-KO IHCs had comparable ΔC_m (Ai) and efficiency of Ca^{2+} current to drive exocytosis, as probed by the ratio of ΔC_m and Q_{Ca} (Aii), in response to 20 ms step depolarization, primarily eliciting RPP release (AP180-KO $n=15$ IHCs, $N=12$ mice; Wt $n=15$ IHCs, $N=11$ mice). (B) Exemplary traces of Ca^{2+} current (top) and C_m (bottom) upon 200 ms step depolarization. ΔC_m in AP180-KO IHCs was comparable with Wt IHCs in response to 200 ms depolarization eliciting sustained release (Bi). The efficiency of Ca^{2+} current to drive exocytosis was comparable (Bii). Average traces of C_m in response to 20 ms (C) and 200 ms (D) depolarization (mean \pm s.e.m., AP180-KO $n=16$ IHCs, $N=12$ mice; Wt $n=17$ IHCs, $N=14$ mice). (E) The time of return to baseline after 20 ms depolarization was comparable between AP180-KO and Wt IHCs. (F) The slope of the slow linear component of endocytic membrane retrieval, most likely reflecting CME, was calculated by fitting a line to the first 20 s of the C_m recording after the depolarization. AP180-KO IHCs showed a shallower slope (without the outliers, $P=0.002$, Student's t -test, with the outliers, $P=0.043$, Mann-Whitney U -test). (G) The slope of the linear component following 200 ms depolarization was not statistically distinguishable. We did not observe significant differences in the amplitude (H) and the time constant (I) of the fast, exponential component of endocytosis, likely to represent bulk endocytosis. The outliers were detected via inter-quartile range (IQR) method and were depicted as filled diamonds. * $P<0.05$; ns, not significant.

AP180 is required for clathrin-dependent endocytosis and SV reformation following bulk retrieval in IHCs

The reduced rate of endocytic C_m decline and the reduction of clathrin-coated SVs in resting and stimulated AP180-KO IHCs support a role of AP180 in CME. Beyond that, we observed less budding of CCPs from enlarged ELVs in AP180-KO IHCs after high- K^+ stimulation, suggesting that SV reformation from ELVs following bulk retrieval operates in an AP180-dependent manner.

Clathrin-dependent SV reformation from ELVs was also impaired in AP-2 KO IHCs (Jung et al., 2015a). Therefore, like in hippocampal neurons (Kononenko et al., 2014; Koo et al., 2015), both adaptor proteins seem to be required for the recruitment of clathrin triskelia not only to the plasma membrane, but also to ELVs. Notably, SV numbers were more robustly reduced in AP180-deficient IHCs ($\sim 60\%$) than in AP180-deficient inhibitory CNS neurons ($\sim 33\%$; note that no SV reduction was found in excitatory neurons, Koo

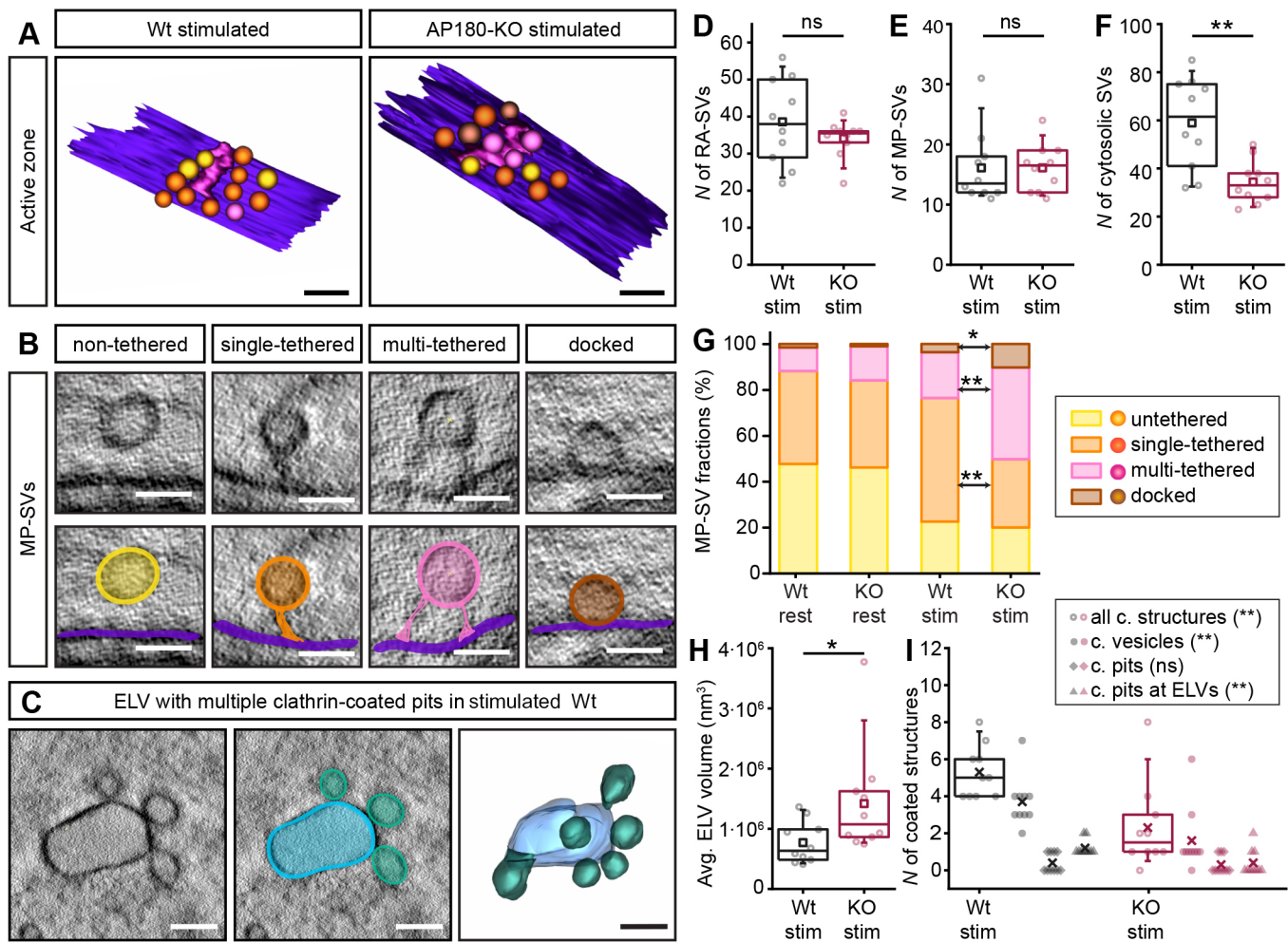


Fig. 7. SV tethering to the AZ and SV reformation are altered in stimulated IHCs from AP180-KO mice. (A) Reconstructed models of the AZ from P15 Wt and AP180-KO IHCs after 5 min K^+ stimulation showing the presynaptic density and MP-SVs. Colors of different classes of MP-SVs are as highlighted in B. Scale bars: 200 nm. (B) Exemplary virtual sections of MP-SVs in untethered, tethered or docked state. Scale bars: 50 nm. (C) Virtual section and 3D model of an ELV containing multiple CCPs, as exclusively observed in Wt. Scale bars: 100 nm. (D) Numbers (N) of RA-SVs were unaltered in P15 AP180-KO mice compared to Wt (n for D-I=10 tomograms from two different animals per group). (E) The number of MP-SVs was likewise unaltered in absence of AP180 compared to Wt, whereas numbers of small uncoated vesicles were strongly reduced (F). (G) Examining numbers of tethers, a significantly higher proportion of multi-tethered and docked MP-SVs have been observed combined with a relatively lower number of single-tethered SVs in absence of AP180 after stimulation compared to stimulated Wt as well as compared to resting condition in Wt and AP180-KO. (H) The volume of ELVs was increased in the AP180-KO mice. (I) Numbers of coated structures were decreased with numbers of coated vesicles and coated pits at ELVs being most strongly affected. * $P < 0.05$; ** $P < 0.01$; ns, not significant.

et al., 2015). This underlines the importance of clathrin- and AP180-dependent SV reformation from endocytic intermediates for the restoration of SV pools particularly in cells with a high SV turnover rate like the IHCs.

Nonetheless, CME still occurred, and bulk retrieval of membrane seemed unaffected in AP180-deficient IHCs. Moreover, prolonged stimulation by high- K^+ left the RA- and MP-SVs pools unchanged and did not further reduce the number of cytosolic SVs in AP180-KO IHCs. Therefore, AP180-independent forms of membrane retrieval must exist in IHCs, and other adaptor proteins, like the AP180 homolog CALM, AP-2 or AP-3, may contribute to the recruitment of clathrin. The precise interplay of adapter proteins and membrane retrieval mechanisms in IHCs requires further investigation. Also, future studies might address the question of whether accumulation of exocytosed proteins and lipids at the plasma membrane, or increased membrane tension, shift membrane retrieval towards clathrin-independent forms (Maritzen and Haucke, 2018).

A role of AP180 in release site clearance at IHC active zones

Notwithstanding the SV reformation deficit, the number of MP-SVs at the AZ was not significantly reduced in AP180-KO IHCs during strong stimulation. Still, the measured rate of SV replenishment during trains of brief depolarizations was reduced in AP180-KO IHCs, while Ca^{2+} -triggered fusion of the RRP of SVs seemed intact. These findings suggest that slowed SV replenishment of the release sites was primarily due to impaired AZ clearance rather than to insufficient SV resupply to the AZ. Effective release site clearance has previously been discussed as a determinant of sustained exocytosis in hair cells (Pangršič et al., 2010; Cho et al., 2011; Jung et al., 2015; Chakrabarti et al., 2018; Kroll et al., 2019). Further support for this hypothesis comes from the observation of an increased number of multi-tethered and docked SVs in the AP180-KO IHCs. Similarly, in IHCs of the otoferlin mouse mutant *pachanga*, which has been shown to be profoundly deaf with a reduced rate of SV replenishment to the RRP (Pangršič et al., 2010), the number of multi-tethered SVs was significantly higher than in Wt

after stimulation (Chakrabarti et al., 2018). Multi-tethered SVs in neurons were also shown to be closer to the AZ membrane compared to single-tethered or untethered SVs, and probably display a prerequisite for SV docking and priming (Fernández-Busnadiego et al., 2013). As SV fusion was intact in AP180-KO IHCs, we take the higher prevalence of multi-tethered SVs as a potential morphological correlate of unproductive release sites due to impaired clearance.

In a previous study, absence of RIM-binding protein 2 (RIM-BP2) likewise resulted in an increased distance of MP-SVs to the AZ-membrane in IHCs at resting conditions, which has been attributed to disturbances in the composition of the cytomatrix of the AZ (Krinner et al., 2017). Changes in the cytomatrix or in the AZ plasma membrane itself may also serve as an explanation for the increased distance of MP-SVs in absence of AP180. More precisely, the absence of AP180 could lead to an accumulation of proteins or lipids at the membrane of the release sites, which possibly causes an energetically unfavorable environment, ultimately slowing down exocytic processes after prolonged stimulation.

AP180 has previously been identified as a key sorting factor for VAMP2. Consequently, AP180 deficiency causes an accumulation of VAMP2 at the plasma membrane of neurons (Koo et al., 2015). Even though IHCs seem to operate without VAMP2 and other neuronal SNARE proteins (Nouvian et al., 2011), AP180 could be required for the sorting of other members of the VAMP family that were previously identified as additional interaction partners of AP180 or CALM (Maritzen et al., 2012; Miller et al., 2011; Sahlender et al., 2013). Alternatively, an as-yet-unknown exocytic IHC protein may interact with AP180 and accumulate at the plasma membrane in the absence of AP180. Importantly, unaltered otoferlin levels suggest that otoferlin sorting does not depend on AP180 and consequently allow us to attribute the IHC phenotype to AP180 deficiency itself rather than to a concomitant loss of otoferlin.

MATERIALS AND METHODS

Animals

Constitutive knockout mice for AP180 as well as their wild-type littermates, as previously described in Koo et al. (2015), were used in this study. For all experiments, mice of either sex were examined shortly after the onset of hearing (P14–P18). For the analysis of AP180 localization and distribution, C57BL6/J mice were used. All experiments complied with national animal care guidelines and were approved by the University Medical Center Göttingen board for animal welfare and the animal welfare office of the state of Lower Saxony.

Immunohistochemistry and confocal microscopy

Freshly dissected apical turns of organs of Corti from 2-week-old mice were (1) chemically stimulated for 1 min using high- K^+ stimulation solution (65.36 mM KCl, 79.7 mM NaCl, 2 mM $CaCl_2$, 1 mM $MgCl_2$, 0.5 mM $MgSO_4$, 10 mM HEPES, 3.4 mM L-glutamine, and 6.9 mM D-glucose, pH 7.4) or incubated in a high Ca^{2+} , low K^+ solution for control (5.36 mM KCl, 139.7 mM NaCl, 2 mM $CaCl_2$, 1 mM $MgCl_2$, 0.5 mM $MgSO_4$, 10 mM HEPES, 3.4 mM L-glutamine, and 6.9 mM D-glucose, pH 7.4; see also Revelo et al., 2014) at room temperature followed by fixation using 4% formaldehyde (FA) in phosphate-buffered saline (PBS) on ice, or (2) were directly fixed with 4% FA in PBS for 10 min (for RIBEYE/CtBP2 and Homer1) or for 60 min (for otoferlin, Vglut3 and AP180) on ice. After three 10 min washing steps in PBS, blocking solution [goat serum dilution buffer (GSDB); 16% normal goat serum, 450 mM NaCl, 0.3% Triton X-100, 20 mM phosphate buffer, pH 7.4] was applied for 1 h in a wet chamber at room temperature. Primary antibodies were diluted in GSDB and applied overnight at 4°C in a wet chamber. After three 10 min washes (wash buffer, 450 mM NaCl, 20 mM phosphate buffer, 0.3% Triton X-100), secondary antibodies diluted in GSDB were applied in a light-protected wet chamber for 1 h at room temperature. Then, the specimens were washed three times in wash buffer and finally in 5 mM phosphate buffer and mounted onto glass microscope slides with mounting medium (Mowiol 4-88, Sigma-Aldrich).

The following primary antibodies were used: rabbit anti-AP180 (1:300, Synaptic Systems, cat. No. 155 003), mouse anti-CtBP2 (also recognizing the ribbon protein ribeye, 1:200, BD Biosciences, cat. no. 612044), mouse anti-otoferlin (1:300, Abcam, cat. no. ab53233), rabbit anti-Vglut3 (1:300, Synaptic Systems, cat. no. 135 203), rabbit anti-Homer1 (1:200, Synaptic Systems, cat. No. 160 002) and guinea pig anti-synapsin1/2 (Synaptic Systems, cat. no. 106 002). The secondary antibodies used for confocal microscopy were goat anti-rabbit-IgG conjugated to Alexa Fluor 488 (1:200, Invitrogen, cat. No. A 11008), goat anti-mouse-IgG conjugated to Alexa Fluor 568 (1:200, Invitrogen, cat. No. A11004), goat anti-mouse-IgG conjugated to Alexa Fluor 633 (1:200, Invitrogen, cat. no. A21136), and goat anti-guinea pig-IgG conjugated to Alexa Fluor 568 (1:200, Invitrogen, cat. no. A11075). Confocal images were acquired using a laser scanning confocal microscope (Zeiss LSM800, Carl Zeiss AG, Oberkochen, Germany) with 488 nm (Ar) and 561 nm (He-Ne) lasers for excitation and 1.4 NA 63× oil immersion objectives. z-axis stacks of 2D images were generated with a step size of 0.6 μm from comparable tonotopic regions. Images were processed using ImageJ (<http://imagej.net/>) and assembled for display in Adobe Illustrator software. For semiquantitative analysis of immunofluorescence, samples of AP180-KO and control/unstimulated and stimulated probes were processed identically and in parallel throughout immunohistochemistry, confocal imaging and analysis.

Quantitative RT-PCR

Total RNA was isolated from the cochlea of 12–14-day-old mice using the PureLink™ RNA Mini Kit in combination with Trizol (Thermo Fisher Scientific). The SuperScript® IV First-Strand Synthesis System (Thermo Fisher Scientific) was used to obtain cDNA according to manufacturer's instructions using oligo(dT) primers and random hexamers. Quantitative RT-PCR (qPCR) was performed using a PowerUP SYBR™ Green master mix and gene-specific primers for Vglut3 and otoferlin (see Table S2 for primer sequences). The StepOne™ Real-Time PCR System (Thermo Fisher Scientific) was used to perform qPCR. Each PCR was repeated three times in one experimental run.

High-pressure freezing and freeze substitution

High-pressure freezing (HPF) and freeze substitution (FS) were essentially performed as described previously (Chakrabarti et al., 2018; Jung et al., 2015b; Wong et al., 2014). Briefly, for HPF, the apical cochlear turns from P15–P16 Wt and AP180-KO mice were dissected in Ca^{2+} -free Hanks' balanced salt solution (HBSS) and carefully placed on aluminium specimen carriers in the 0.2 mm cavity (type A, 0.1 and 0.2 mm cavity, Leica Microsystems, Wetzlar, Germany) filled with HBSS solution. A second specimen carrier (0.3 mm cavity, type B, Leica Microsystems) was dipped in hexadecane and placed onto the first specimen carrier with the cavity upwards. An HPM100 (Leica Microsystems) high-pressure freezer was used for sample freezing. Immediately afterwards, samples were transferred into liquid nitrogen and stored until freeze substitution was performed. For stimulation, organs of Corti were dissected in Ca^{2+} -free HBSS solution and transferred into stimulation solution (identical with the solution used for immunohistochemistry experiments). Within the stimulation solution, samples were placed on specimen carriers and frozen exactly 5 min after the transfer.

Freeze substitution was performed with an AFS2 (Leica Microsystems) freeze substitution device. Organs of Corti were transferred into the AFS2 precooled to $-90^{\circ}C$. After 4 days incubation in 0.1% tannic acid in acetone, samples were washed three times for 1 h each time in acetone before 2% (w/v) osmium tetroxide in acetone was applied at $-90^{\circ}C$. The temperature was increased from $-90^{\circ}C$ to $-20^{\circ}C$ ($5^{\circ}C/h$), maintained at $-20^{\circ}C$ for 17 h and was further increased from $-20^{\circ}C$ to $+4^{\circ}C$ ($10^{\circ}C/h$). Osmium tetroxide was removed at $4^{\circ}C$ and samples were washed three times for 1 h each time with acetone. Subsequently, samples were slowly warmed to room temperature. Finally, organs of Corti were infiltrated with Epon resin [acetone/Epon 1:1 (v/v) for 2 h, 100% Epon overnight], placed into embedding molds and polymerized for 48 h at $70^{\circ}C$.

Electron tomography

Electron tomography of ribbon synapses was performed as described previously (Jung et al., 2015b; Strenzke et al., 2016). 250 nm sections of the

embedded samples were obtained, approaching from the anterior edge, using an ultramicrotome (UC6, Leica Microsystems, Wetzlar, Germany) with a 35° diamond knife (Diatome, Nidau, Switzerland) and applied to formvar-coated copper 75-mesh grids. Sections were post-stained with uranyl acetate replacement solution (Science services, Munich, Germany) for 40 min and lead citrate for 1 min following standard protocols. To both sides of the grids, 10 nm gold beads (British Bio Cell, Crumlin, UK) were applied as fiducial markers. Using Serial-EM software, single tilt series from -60° to +60° (increments of 1°) were acquired with a JEM2100 (JEOL, Freising, Germany) electron microscope at 200 kV and 10,000× magnification. For tomogram generation, the IMOD package etomo was used; models were generated with 3dmod (bio3d.colorado.edu/imod/).

Auditory brainstem recordings and distortion product otoacoustic emissions

ABRs and DPOAE were performed on 6-week-old mice as previously described (Jing et al., 2013). Briefly, mice were anesthetized with a combination of ketamine (125 mg/kg body weight) and xylazine (2.5 mg/kg body weight) through intraperitoneal injection. The core temperature was maintained constant at 37°C using a heat blanket (Hugo Sachs Elektronik–Harvard Apparatus). The TDT II system run by BioSig software was used for stimulus generation, presentation and data acquisition (Tucker Davis Technologies; MathWorks). Tone bursts (as a sequence at 4, 6, 8, 12, 16, 24 and 32 kHz, with 10 ms plateau, 1 ms cos2 rise/fall) or clicks of 0.03 ms were presented at 40 Hz (tone bursts) or 20 Hz (clicks) in the free field ipsilaterally using a JBL 2402 speaker.

Patch-clamp recordings from IHCs

The apical turn of the organs of Corti were acutely dissected from P14 to P18 animals in HEPES Hank's solution containing (in mM): 5.36 KCl, 141.7 NaCl, 10 HEPES, 0.5 MgSO₄·7H₂O, 1 MgCl₂·6H₂O, 5.6 D-glucose, and 3.4 L-glutamine (pH 7.2, ~300 mOsm/l). The IHC basolateral membranes were exposed by cleaning of nearby cells with a suction pipette. IHCs were patch clamped at room temperature (20–25°C) in perforated-patch configuration as described previously (Moser and Beutner, 2000). For Ca²⁺ current and capacitance (C_m) measurements, the extracellular solution contained the following (in mM): 110 NaCl, 35 TEA-Cl, 2.8 KCl, 1 MgCl₂, 1 CsCl, 10 HEPES, 5 CaCl₂, and 11.1 D-glucose (pH 7.2, ~305 mOsm/l) and was introduced into the recording chamber via a perfusion system. The pipette solution contained (in mM): 130 Cs-gluconate, 10 TEA-Cl, 10 4-AP, 10 HEPES, 1 MgCl₂, as well as 300 mg/ml amphotericin B (pH 7.17, ~290 mOsm/l). The measurements were undertaken with EPC-10 amplifiers controlled by Patchmaster software (HEKA Elektronik, Germany). IHCs were held at -84 mV. All voltages were corrected for liquid junction potential offline (14 mV). Currents were leak corrected using a p/10 protocol (Annstrong et al., 1974). Recordings were used only if the leak current was lower than 30 pA and the series resistance (R_s) was lower than 30 MΩ. Recordings were discarded when the Ca²⁺ current rundown exceeded 25%.

For current–voltage (*I*–*V*) recordings, the IHCs were step depolarized for 10 ms to -14 mV from the holding potential of -84 mV to +63 mV in 5 mV increments. For C_m measurements, IHCs were stimulated by step depolarizations to -14 mV for durations of 20 or 200 ms at intervals of 60–100 s. The Lindau–Neher technique was used to measure the capacitance changes (Lindau and Neher, 1988). Exocytosis and endocytosis were quantified from C_m changes (ΔC_m) as described previously (Neef et al., 2014).

Data analysis

Immunohistochemistry

The intensities of AP180, otoferlin and synapsin1/2 fluorescence signals along the longitudinal axis of IHCs (Fig. 1) were measured via line profiles using ImageJ software. Igor Pro 6.3 software was used to generate average intensity profiles. The distribution of AP180 in the cytosol and its membrane proximity was assessed from intensity line scans reaching from the basal plasma membrane towards the cytosol along the longitudinal axis of IHCs (Fig. S1C–C_{ii}) and from a high-intensity fluorescence cluster analysis (Fig. S1D–D_i) performed using ImageJ software. To do this, middle planes of IHCs were selected and cell borders were defined via otoferlin co-staining. In the otoferlin channel, lines from the cell membrane towards

the nucleus were drawn and fluorescence intensity was measured in the AP180 channel (pixel intensity values ranging from 0 to 255) to avoid bias. Igor Pro 6.3 software was used to generate average intensity profiles of the individual cells. Separated clusters of high AP180 immunofluorescence intensity were defined by application of an intensity threshold (the threshold was adjusted once for clusters in a stimulated example image and then used for all images) using ImageJ software. Within each IHC (as defined by otoferlin co-staining), the average size and mean intensity of all clusters were calculated using the ImageJ tool 'analyze particles'. Only clusters with a size of ≥0.04 μm² were included because of the resolution limit of confocal microscopy (~200–250 nm for the used fluorophores here). IHC ribbon synapses were manually counted in *z*-projections of confocal sections from RIBEYE/CtBP2 and Homer1 immunolabeled organs of Corti using ImageJ software. Otoferlin and Vglut3 levels of IHCs were semi-quantitatively assessed as immunofluorescence intensity values and analyzed using Imaris (Bitplane) and Matlab (Mathworks), as described previously (Strenzke et al., 2016). Intensities of each cell are normalized to the average intensity of the Wt group for otoferlin or for Vglut3.

qPCR

StepOne™ Real-Time PCR System software was used to analyze qPCR results. Relative quantification values were calculated by comparative C_T method. *Hprt* was used as a housekeeping gene.

Electron tomography

Only tomograms with a single ribbon synapse clearly anchored to the AZ were selected for quantification using the IMOD package 3dmod (<http://bio3d.colorado.edu/imod/>) and as described previously (Chakrabarti et al., 2018; Kroll et al., 2019). Small, clear vesicles were classified as synaptic vesicles (SVs) if they appeared round and if their outer diameter (defined by fitting a circle to the borders at the maximum projection of the respective SV) was smaller than 70 nm. SVs were categorized as belonging to one of three groups: (1) ribbon-associated SVs (RA-SVs) if they were located in the first row around the synaptic ribbon and with a maximum distance of 80 nm from the ribbon, (2) membrane-proximal SVs (MP-SVs) if the distance between SV and plasma membrane was less than 50 nm and if the distance between SV and presynaptic density was less than 100 nm, and (3) cytosolic SVs if the distance between SV and ribbon was less than 500 nm thereby excluding RA-SVs and MP-SVs (all criteria being valid at maximum projection of the respective SV). MP-SVs were further subdivided into four groups depending on their connection to the AZ plasma membrane as described in a previous study (Chakrabarti et al., 2018). SVs were counted as docked if the distance between SV outer membrane and AZ membrane was 0–2 nm. Single-tethered SVs were defined as all SVs with only one tether reaching from the SV to the AZ membrane. Multi-tethered SVs were defined as all SVs with more than one tether from the SV to the AZ membrane. SVs were categorized as untethered if no filament was observed between SV and plasma membrane (thereby ignoring possible filamentous connections between SVs, as well as between SVs and presynaptic density or between SV and ribbon). Furthermore, all structures containing a clathrin coat were counted as coated structures if the minimal distance between organelle and ribbon was less than 500 nm. This quantification includes structures with a coat around the entire clathrin-coated SV (independent of its size), coated pits budding from the plasma membrane and endosome-like vacuoles (ELVs) with at least one budding coated pit (in this case, the ELV with pit was only counted once and not included in the additional ELV quantification). All membranous organelles were defined as ELVs and counted if their maximum diameter was larger than 70 nm and/or if they were tubular, and if the minimal distance between ELV and ribbon was less than 500 nm. The volume of each ELV was assessed from a modeled mesh calculated from contours drawn in every virtual section of the ELV in 3dmod.

Patch-clamp recordings

Electrophysiological data was analyzed with custom-written programs in Igor Pro 6.3 and Python (available upon request). For the analysis of the *I*–*V* curves, the final 5 ms of the evoked Ca²⁺ currents were averaged after subtracting the mean of the first 5 ms of the recording. For the analysis of the stimuli train, 70 ms of C_m was averaged to calculate exocytic Cm increments

(ΔC_m) skipping the first 50 ms after each depolarization to avoid impact of non-exocytic C_m transients. In order to estimate the replenishment rate of SVs, we undertook 'SMN analysis' as described previously (Schneeggenburger et al., 1999). We plotted cumulative ΔC_m versus the stimulus number. A line was fitted to the last five points, and the slope of the fit was taken as the replenishment rate. We furthermore calculated the replenishment rate in terms of vesicles per stimulus. We used the diameter values obtained from the tomograms of Wt and AP180-KO IHCs, subtracting the mean membrane thickness (Neef et al., 2007) to obtain the mid-membrane diameter. For the conversion of SV diameter to capacitance values, a specific capacitance value of $9.1 \text{ fF}\mu\text{m}^{-2}$ (Albillos et al., 1997) was used and spherical shape was assumed.

For calculating the ΔC_m , the difference between the mean 400 ms C_m before and 200 ms after the depolarization was taken. The Ca^{2+} charge (Q_{Ca}) was calculated by taking the integral of the leak-subtracted current during depolarization. The endocytosis recordings were analyzed as described previously (Neef et al., 2014). The overall observed decrease in C_m during perforated patch-clamp recordings were corrected by using the slope of the global fit to C_m values taken from each recording. We calculated the slow component of the endocytosis by a linear fit of post-depolarization C_m , skipping the first 200 ms. Recordings that did not return to baseline within 80 s were excluded from the analysis. The amplitude of the exponential component of C_m decline after 200 ms depolarization was calculated by subtraction of linear fit to final 15 s of C_m . An exponential function was fit to the residual C_m using a genetic curve-fitting algorithm (Sanchez del Rio and Pareschi, 2001). IHCs that did not exhibit exponential component were excluded from the analysis.

Statistical analysis

Sample sizes were chosen according to typical observation numbers used in each respective field and can be found in the respective figures and/or corresponding figure legends. For quantification, the following software was used: MATLAB (Mathworks), Excel (Microsoft), Igor Pro 6 (Wavemetrics), Origin 9.0 (Microcal Software), GraphPad Prism (GraphPad Software) and Python. Averages are expressed as mean \pm s.e.m., boxes in box plots show the 25–75 quartiles with the median, whiskers extend from the 10th–90th percentile; the mean is indicated by a square or cross. Data sets were tested for normal distribution (D'Agostino and Pearson omnibus normality test for electron microscopy and immunohistochemistry with GraphPad Prism software, and for functional data with Python) and equality of variances (F test). Statistical significance was calculated using an unpaired, two-tailed Student's t -test for normally distributed data, a Mann–Whitney U -test for non-normally distributed data and Kolmogorov–Smirnov test to compare data distribution. For Fig. 7G, one-way ANOVA (two-way ANOVA for Fig. 2B) followed by Tukey's post-hoc test was used to compare multiple groups. Significant differences are reported as $*P<0.05$, $**P<0.01$ and $***P<0.001$.

Acknowledgements

We thank N. Dietrich, S. Thom, A. Goldak, S. Gerke, and C. Senger-Freitag for expert technical assistance. N. Dietrich performed most ABR and DPOAE measurements. We thank Dr J. Neef for his help with patch-clamp and confocal microscopy analysis. We would like to thank Dr F. Schmitz for providing animals and Dr Vladan Rankovic for help with the RT-PCR experiments.

Competing interests

The authors declare no competing or financial interests.

Author contributions

Conceptualization: J.K., Ö.D.Ö., C.W., T. Moser; Formal analysis: J.K., Ö.D.Ö.; Investigation: J.K., Ö.D.Ö., S.J.; Resources: T. Maritzen; Writing - original draft: J.K., T. Moser; Writing - review & editing: J.K., Ö.D.Ö., S.J., T. Maritzen, I.M., C.W., T. Moser; Visualization: J.K., Ö.D.Ö.; Supervision: I.M., C.W., T. Moser; Project administration: C.W., T. Moser; Funding acquisition: I.M., C.W., T. Moser.

Funding

This work was supported by grants of the Deutsche Forschungsgemeinschaft (German Research Foundation) through the collaborative research center 889 (project A8 to I.M. and T.M. and A7 to C.W.), the Emmy-Noether program (to I.M.) and the Leibniz program (to T.M.).

Supplementary information

Supplementary information available online at <http://jcs.biologists.org/lookup/doi/10.1242/jcs.236737.supplemental>

References

- Albillos, A., Dernick, G., Horstmann, H., Almers, W., Alvarez de Toledo, G. and Lindau, M. (1997). The exocytotic event in chromaffin cells revealed by patch amperometry. *Nature* **389**, 509–512. doi:10.1038/39081
- Annstrong, C. M., and Bezanilla, F. (1974). Charge movement associated with the opening and closing of the activation gates of the sodium channel. *J. Gen. Physiol.* **63**, 533–552. doi:10.1085/jgp.63.5.533
- Becker, L., Schnee, M. E., Niwa, M., Sun, W., Maxeiner, S., Talaei, S., Kachar, B., Rutherford, M. A. and Ricci, A. J. (2018). The presynaptic ribbon maintains vesicle populations at the hair cell afferent fiber synapse. *eLife* **7**, e30241. doi:10.7554/eLife.30241
- Boumil, R. M., Letts, V. A., Roberts, M. C., Lenz, C., Mahaffey, C. L., Zhang, Z., Moser, T. and Frankel, W. N. (2010). A missense mutation in a highly conserved alternate exon of dynamin-1 causes epilepsy in fitful mice. *PLoS Genet.* **6**, e1001046. doi:10.1371/journal.pgen.1001046
- Chakrabarti, R., Michanski, S. and Wichmann, C. (2018). Vesicle sub-pool organization at inner hair cell ribbon synapses. *EMBO Rep.* **19**, e44937. doi:10.15252/embr.201744937
- Cho, S., Li, G. L. and von Gersdorff, H. (2011). Recovery from short-term depression and facilitation is ultrafast and Ca^{2+} dependent at auditory hair cell synapses. *J. Neurosci.* **31**, 5682–5692. doi:10.1523/JNEUROSCI.5453-10.2011
- Cousin, M. A. (2017). Integration of synaptic vesicle cargo retrieval with endocytosis at central nerve terminals. *Front. Cell. Neurosci.* **11**. doi:10.3389/fncel.2017.00234
- Duncker, S. V., Franz, C., Kuhn, S., Schulte, U., Campanelli, D., Brandt, N., Hirt, B., Fakler, B., Blin, N., Ruth, P. et al. (2013). Otoferlin couples to clathrin-mediated endocytosis in mature cochlear inner hair cells. *J. Neurosci.* **33**, 9508–9519. doi:10.1523/JNEUROSCI.5689-12.2013
- Fernández-Busnadiego, R., Asano, S., Oprisoreanu, A.-M., Sakata, E., Doengi, M., Kochovski, Z., Zürner, M., Stein, V., Schoch, S., Baumeister, W. et al. (2013). Cryo-electron tomography reveals a critical role of RIM1 α in synaptic vesicle tethering. *J. Cell Biol.* **201**, 725–740. doi:10.1083/jcb.201206063
- Ford, M. G. J., Pearse, B. M. F., Higgins, M. K., Vallis, Y., Owen, D. J., Gibson, A., Hopkins, C. R., Evans, P. R. and McMahon, H. T. (2001). Simultaneous binding of PtdIns(4,5)P₂ and clathrin by AP180 in the nucleation of clathrin lattices on membranes. *Science* **291**, 1051–1055. doi:10.1126/science.291.5506.1051
- Grabner, C. P. and Moser, T. (2018). Individual synaptic vesicles mediate stimulated exocytosis from cochlear inner hair cells. *Proc. Natl. Acad. Sci. USA* **115**, 12811–12816. doi:10.1073/pnas.1811814115
- Hao, W., Luo, Z., Zheng, L., Prasad, K. and Lafer, E. M. (1999). AP180 and AP-2 interact directly in a complex that cooperatively assembles clathrin. *J. Biol. Chem.* **274**, 22785–22794. doi:10.1074/jbc.274.32.22785
- Hauke, V., Neher, E. and Sigrist, S. J. (2011). Protein scaffolds in the coupling of synaptic exocytosis and endocytosis. *Nat. Rev. Neurosci.* **12**, 127–138. doi:10.1038/nrn2948
- Imig, C., Min, S.-W., Krunner, S., Arancillo, M., Rosenmund, C., Südhof, T. C., Rhee, J. S., Brose, N. and Cooper, B. H. (2014). The morphological and molecular nature of synaptic vesicle priming at presynaptic active zones. *Neuron* **84**, 416–431. doi:10.1016/j.neuron.2014.10.009
- Jean, P., Lopez de la Morena, D., Michanski, S., Tobón, L. M. J., Chakrabarti, R., Picher, M. M., Neef, J., Jung, S. Y., Gültas, M., Maxeiner, S. et al. (2018). The synaptic ribbon is critical for sound encoding at high rates and with temporal precision. *eLife Sci.* **7**, e29275. doi:10.7554/eLife.29275
- Jing, Z., Rutherford, M. A., Takago, H., Frank, T., Fejtova, A., Khimich, D., Moser, T. and Strenzke, N. (2013). Disruption of the presynaptic cytomatrix protein bassoon degrades ribbon anchorage, multiquantal release, and sound encoding at the hair cell afferent synapse. *J. Neurosci.* **33**, 4456–4467. doi:10.1523/JNEUROSCI.3491-12.2013
- Johnson, C. P. and Chapman, E. R. (2010). Otoferlin is a calcium sensor that directly regulates SNARE-mediated membrane fusion. *J. Cell Biol.* **191**, 187–197. doi:10.1083/jcb.201002089
- Jung, S. Y., Maritzen, T., Wichmann, C., Jing, Z., Neef, A., Revelo, N. H., Al-Moyed, H., Meese, S., Wojcik, S. M., Panou, I. et al. (2015a). Disruption of adaptor protein 2 μ (AP-2 μ) in cochlear hair cells impairs vesicle reloading of synaptic release sites and hearing. *EMBO J.* **34**, 2686–2702. doi:10.15252/emj.2015191885
- Jung, S., Oshima-Takago, T., Chakrabarti, R., Wong, A. B., Jing, Z., Yamanbaeva, G., Picher, M. M., Wojcik, S. M., Göttfert, F., Predehlf, F. et al. (2015b). Rab3-interacting molecules 2 α and 2 β promote the abundance of voltage-gated $\text{CaV}1.3 \text{ Ca}^{2+}$ channels at hair cell active zones. *Proc. Natl. Acad. Sci. USA* **112**, E3141–E3149. doi:10.1073/pnas.1417207112
- Khimich, D., Nouvian, R., Pujol, R., Tom Dieck, S., Egner, A., Gundelfinger, E. D. and Moser, T. (2005). Hair cell synaptic ribbons are essential for synchronous auditory signalling. *Nature* **434**, 889–894. doi:10.1038/nature03418

- Kononenko, N. L., Puchkov, D., Classen, G. A., Walter, A. M., Pechstein, A., Sawade, L., Kaempf, N., Trimbuch, T., Lorenz, D., Rosenmund, C. et al. (2014). Clathrin/AP-2 mediate synaptic vesicle reformation from endosome-like vacuoles but are not essential for membrane retrieval at central synapses. *Neuron* **82**, 981-988. doi:10.1016/j.neuron.2014.05.007
- Koo, S. J., Markovic, S., Puchkov, D., Mahrenholz, C. C., Beceren-Braun, F., Maritzen, T., Darnedde, J., Volkmer, R., Oschkinat, H. and Haucke, V. (2011). SNARE motif-mediated sorting of synaptobrevin by the endocytic adaptors clathrin assembly lymphoid myeloid leukemia (CALM) and AP180 at synapses. *Proc. Natl Acad. Sci. USA* **108**, 13540-13545. doi:10.1073/pnas.1107067108
- Koo, S. J., Kochlamazashvili, G., Rost, B., Puchkov, D., Gimber, N., Lehmann, M., Tadeus, G., Schmoranzler, J., Rosenmund, C., Haucke, V. et al. (2015). Vesicular synaptobrevin/VAMP2 levels guarded by AP180 control efficient neurotransmission. *Neuron* **88**, 330-344. doi:10.1016/j.neuron.2015.08.034
- Krinner, S., Butola, T., Jung, S., Wichmann, C. and Moser, T. (2017). RIM-binding protein 2 promotes a large number of CaV1.3 Ca²⁺-channels and contributes to fast synaptic vesicle replenishment at hair cell active zones. *Front. Cell Neurosci.* **11**, 334. doi:10.3389/fncel.2017.00334
- Kroll, J., Jaime Tobón, L. M., Vogl, C., Neef, J., Kondratiuk, I., König, M., Strenzke, N., Wichmann, C., Milosevic, I. and Moser, T. (2019). Endophilin-A regulates presynaptic Ca²⁺ influx and synaptic vesicle recycling in auditory hair cells. *EMBO J.* **38**, e100116. doi:10.15252/embj.2018100116
- Lenzi, D., Crum, J., Ellisman, M. H. and Roberts, W. M. (2002). Depolarization redistributes synaptic membrane and creates a gradient of vesicles on the synaptic body at a ribbon synapse. *Neuron* **36**, 649-659. doi:10.1016/S0896-6273(02)01025-5
- Lindau, M. and Neher, E. (1988). Patch-clamp techniques for time-resolved capacitance measurements in single cells. *Pflügers Arch. Eur. J. Physiol.* **411**, 137-146. doi:10.1007/BF00582306
- Lindner, R. and Ungewickell, E. (1992). Clathrin-associated proteins of bovine brain coated vesicles. An analysis of their number and assembly-promoting activity. *J. Biol. Chem.* **267**, 16567-16573.
- Lv, C., Stewart, W. J., Akanyeti, O., Frederick, C., Zhu, J., Santos-Sacchi, J., Sheets, L., Liao, J. C. and Zenisek, D. (2016). Synaptic ribbons require ribeye for electron density, proper synaptic localization, and recruitment of calcium channels. *Cell Rep.* **15**, 2784-2795. doi:10.1016/j.celrep.2016.05.045
- Maritzen, T. and Haucke, V. (2018). Coupling of exocytosis and endocytosis at the presynaptic active zone. *Neurosci. Res.* **127**, 45-52. doi:10.1016/j.neures.2017.09.013
- Maritzen, T., Koo, S. J. and Haucke, V. (2012). Turning CALM into excitement: AP180 and CALM in endocytosis and disease. *Biol. Cell* **104**, 588-602. doi:10.1111/boc.201200008
- Maxeiner, S., Luo, F., Tan, A., Schmitz, F. and Südhof, T. C. (2016). How to make a synaptic ribbon: RIBEYE deletion abolishes ribbons in retinal synapses and disrupts neurotransmitter release. *EMBO J.* **35**, 1098-1114. doi:10.15252/embj.201592701
- Michalski, N., Goutman, J. D., Auclair, S. M., Boutet de Monvel, J., Tertrais, M., Emptoz, A., Parrin, A., Nouaille, S., Guillon, M., Sachse, M. et al. (2017). Otoferlin acts as a Ca²⁺ sensor for vesicle fusion and vesicle pool replenishment at auditory hair cell ribbon synapses. *eLife Sci.* **6**, e31013. doi:10.7554/eLife.31013
- Miller, S. E., Sahlender, D. A., Graham, S. C., Höning, S., Robinson, M. S., Peden, A. A. and Owen, D. J. (2011). The molecular basis for the endocytosis of small R-SNAREs by the clathrin adaptor CALM. *Cell* **147**, 1118-1131. doi:10.1016/j.cell.2011.10.038
- Morris, S. A., Schröder, S., Plessmann, U., Weber, K. and Ungewickell, E. (1993). Clathrin assembly protein AP180: primary structure, domain organization and identification of a clathrin binding site. *EMBO J.* **12**, 667-675. doi:10.1002/j.1460-2075.1993.tb05700.x
- Moser, T. and Beutner, D. (2000). Kinetics of exocytosis and endocytosis at the cochlear inner hair cell afferent synapse of the mouse. *Proc. Natl. Acad. Sci. USA* **97**, 883-888. doi:10.1073/pnas.97.2.883
- Moser, T., Grabner, C. P. and Schmitz, F. (2019). Sensory processing at ribbon synapses in the retina and the cochlea. *Physiol. Rev.* **100**, 103-144. doi:10.1152/physrev.00026.2018
- Moshkabaranyans, L., Xue, J., Wark, J. R., Robinson, P. J. and Graham, M. E. (2016). A novel sequence in AP180 and CALM promotes efficient clathrin binding and assembly. *PLoS ONE* **11**, e0162050. doi:10.1371/journal.pone.0162050
- Neef, A., Khimich, D., Pirih, P., Riedel, D., Wolf, F. and Moser, T. (2007). Probing the mechanism of exocytosis at the hair cell ribbon synapse. *J. Neurosci.* **27**, 12933-12944. doi:10.1523/JNEUROSCI.1996-07.2007
- Neef, J., Jung, S. Y., Wong, A. B., Reuter, K., Pangršič, T., Chakrabarti, R., Kügler, S., Lenz, C., Nouvian, R., Boumil, R. M. et al. (2014). Modes and regulation of endocytic membrane retrieval in mouse auditory hair cells. *J. Neurosci.* **34**, 705-716. doi:10.1523/JNEUROSCI.3313-13.2014
- Neher, E. and Sakaba, T. (2008). Multiple roles of calcium ions in the regulation of neurotransmitter release. *Neuron* **59**, 861-872. doi:10.1016/j.neuron.2008.08.019
- Nonet, M. L., Holgado, A. M., Brewer, F., Serpe, C. J., Norbeck, B. A., Holleran, J., Wei, L., Hartwig, E., Jorgensen, E. M. and Alfonso, A. (1999). UNC-11, a *Caenorhabditis elegans* AP180 homologue, regulates the size and protein composition of synaptic vesicles. *MBoC* **10**, 2343-2360. doi:10.1091/mbc.10.7.2343
- Nouvian, R., Neef, J., Bulankina, A. V., Reisinger, E., Pangršič, T., Frank, T., Sikorra, S., Brose, N., Binz, T. and Moser, T. (2011). Exocytosis at the hair cell ribbon synapse apparently operates without neuronal SNARE proteins. *Nat. Neurosci.* **14**, 411-413. doi:10.1038/nn.2774
- Pangršič, T., Lasarow, L., Reuter, K., Takago, H., Schwander, M., Riedel, D., Frank, T., Tarantino, L. M., Bailey, J. S., Strenzke, N. et al. (2010). Hearing requires otoferlin-dependent efficient replenishment of synaptic vesicles in hair cells. *Nat. Neurosci.* **13**, 869-876. doi:10.1038/nn.2578
- Pangršič, T., Reisinger, E. and Moser, T. (2012). Otoferlin: a multi-C-2 domain protein essential for hearing. *Trends Neurosci.* **35**, 671-680. doi:10.1016/j.tins.2012.08.002
- Revelo, N. H., Kamin, D., Truckenbrodt, S., Wong, A. B., Reuter-Jessen, K., Reisinger, E., Moser, T. and Rizzoli, S. O. (2014). A new probe for super-resolution imaging of membranes elucidates trafficking pathways. *J. Cell Biol.* **205**, 591-606. doi:10.1083/jcb.201402066
- Roux, I., Safieddine, S., Nouvian, R., Grati, M., Simmler, M.-C., Bahloul, A., Perfettini, I., Le Gall, M., Rostaing, P., Hamard, G. et al. (2006). Otoferlin, defective in a human deafness form, is essential for exocytosis at the auditory ribbon synapse. *Cell* **127**, 277-289. doi:10.1016/j.cell.2006.08.040
- Rutherford, M. A. and Moser, T. (2016). The ribbon synapse between type I spiral ganglion neurons and inner hair cells. In *The Primary Auditory Neurons of the Mammalian Cochlea* (ed. A. Dabdoub, B. Fritzsche, A. N. Popper and R. R. Fay), pp. 117-156. New York: Springer.
- Safieddine, S., El-Amraoui, A. and Petit, C. (2012). The auditory hair cell ribbon synapse: from assembly to function. *Annu. Rev. Neurosci.* **35**, 509-528. doi:10.1146/annurev-neuro-061010-113705
- Sahlender, D. A., Kozik, P., Miller, S. E., Peden, A. A. and Robinson, M. S. (2013). Uncoupling the functions of CALM in VAMP sorting and clathrin-coated pit formation. *PLoS ONE* **8**, e64514. doi:10.1371/journal.pone.0064514
- Sanchez del Rio, M. and Pareschi, G. (2001). Global optimization and reflectivity data fitting for x-ray multilayer mirrors by means of genetic algorithms. *SPIE Proceedings*, 88-96.
- Schmitz, F., Königstorfer, A. and Südhof, T. C. (2000). RIBEYE, a component of synaptic ribbons: a protein's journey through evolution provides insight into synaptic ribbon function. *Neuron* **28**, 857-872. doi:10.1016/S0896-6273(00)00159-8
- Schneggenburger, R., Meyer, A. C. and Neher, E. (1999). Released fraction and total size of a pool of immediately available transmitter quanta at a calyx synapse. *Neuron* **23**, 399-409. doi:10.1016/S0896-6273(00)80789-8
- Siegel, J. H. and Brownell, W. E. (1986). Synaptic and Golgi membrane recycling in cochlear hair cells. *J. Neurocytol.* **15**, 311-328. doi:10.1007/BF01611434
- Strenzke, N., Chakrabarti, R., Al-Moyed, H., Müller, A., Hoch, G., Pangrsic, T., Yamanbaeva, G., Lenz, C., Pan, K.-T., Auge, E. et al. (2016). Hair cell synaptic dysfunction, auditory fatigue and thermal sensitivity in otoferlin I5e15Thr mutants. *EMBO J.* **35**, e201694564. doi:10.15252/embj.201694564
- Trapani, J. G., Obholzer, N., Mo, W., Brockerhoff, S. E. and Nicolson, T. (2009). synaptotagmin 1 is required for temporal fidelity of synaptic transmission in hair cells. *PLoS Genet.* **5**, e1000480. doi:10.1371/journal.pgen.1000480
- Vanlandingham, P. A., Barmchi, M. P., Royer, S., Green, R., Bao, H., Reist, N. and Zhang, B. (2014). AP180 couples protein retrieval to clathrin-mediated endocytosis of synaptic vesicles. *Traffic* **15**, 433-450. doi:10.1111/tra.12153
- Vogl, C., Cooper, B. H., Neef, J., Wojcik, S. M., Reim, K., Reisinger, E., Brose, N., Rhee, J.-S., Moser, T. and Wichmann, C. (2015). Unconventional molecular regulation of synaptic vesicle replenishment in cochlear inner hair cells. *J. Cell. Sci.* **128**, 638-644. doi:10.1242/jcs.162099
- Vogl, C., Panou, I., Yamanbaeva, G., Wichmann, C., Mangosing, S. J., Vilardi, F., Indzhukyan, A. A., Pangršič, T., Santarelli, R., Rodriguez-Ballesteros, M. et al. (2016). Tryptophan-rich basic protein (WRB) mediates insertion of the tail-anchored protein otoferlin and is required for hair cell exocytosis and hearing. *EMBO J.* **35**, e201593565. doi:10.15252/embj.201593565
- Wichmann, C. and Moser, T. (2015). Relating structure and function of inner hair cell ribbon synapses. *Cell Tissue Res.* **361**, 95-114. doi:10.1007/s00441-014-2102-7
- Wong, A. B., Rutherford, M. A., Gabrielaitis, M., Pangršič, T., Göttfert, F., Frank, T., Michanski, S., Hell, S., Wolf, F., Wichmann, C. et al. (2014). Developmental refinement of hair cell synapses tightens the coupling of Ca²⁺ influx to exocytosis. *EMBO J.* **33**, 247-264. doi:10.1002/embj.201387110
- Wu, L.-G., Hamid, E., Shin, W. and Chiang, H.-C. (2014). Exocytosis and endocytosis: modes, functions, and coupling mechanisms. *Annu. Rev. Physiol.* **76**, 301-331. doi:10.1146/annurev-physiol-021113-170305
- Yasunaga, S., Grati, M., Cohen-Salmon, M., El-Amraoui, A., Mustapha, M., Salem, N., El-Zir, E., Loiselet, J. and Petit, C. (1999). A mutation in OTOF, encoding otoferlin, a FER-1-like protein, causes DFNB9, a nonsyndromic form of deafness. *Nat. Genet.* **21**, 363-369. doi:10.1038/7693
- Zhang, B., Koh, Y. H., Beckstead, R. B., Budnik, V., Ganetzky, B. and Bellen, H. J. (1998). Synaptic vesicle size and number are regulated by a clathrin adaptor protein required for endocytosis. *Neuron* **21**, 1465-1475. doi:10.1016/S0896-6273(00)80664-9